January 2017

Transit Photometry Of Recently Discovered Hot Jupiters

Sean Peter Mccloat

TRANSIT PHOTOMETRY OF RECENTLY DISCOVERED HOT JUPITERS

by

Sean Peter McCloat
Bachelor of Arts, SUNY Geneseo, 2013

A Thesis

Submitted to the Graduate Faculty

of the

University of North Dakota

in partial fulfilment of the requirements

for the degree of

Master of Science

Grand Forks, North Dakota
December
2017

This thesis, submitted by Sean P. McCloat in partial fulfillment of the requirements for the Degree of Master of Science from the University of North Dakota, has been read by the Faculty Advisory Committee under whom the work has been done and is hereby approved.

Dr. Mike Gaffey, Chairperson

Dr. Carolina von Essen,

Dr. Ron Fevig,

Dr. Nels Forsman,

This thesis is being submitted by the appointed advisory committee as having met all of the requirements of the School of Graduate Studies at the University of North Dakota and is hereby approved.

Dr. Grant McGimpsey
Dean of the School of Graduate Studies

December 1, 2017
Date

PERMISSION

Title Transit Photometry of Recently Discovered Hot Jupiters

Department Space Studies

Degree Master of Science

In presenting this thesis in partial fulfilment of the requirements for a graduate degree from the University of North Dakota, I agree that the library of this University shall make it freely available for inspection. I further agree that permission for extensive copying for scholarly purposes may be granted by the professor who supervised my thesis work or, in his absence, by the Chairperson of the department of the dean of the School of Graduate Studies. It is understood that any copying or publication or other use of this thesis or part thereof for financial gain shall not be allowed without my written permission. It is also understood that due recognition shall be given to me and to the University of North Dakota in any scholarly use which may be made of any material in my thesis.

Sean Peter McCloat
November 16, 2017

TABLE OF CONTENTS

LIST OF FIGURES

LIST OF TABLES

ACKNOWLEDGEMENTS

I would like to thank my thesis committee and the North Dakota Space Grant Consortium for their participation in and support of this project. I would like to extend an extra-special thank you and my deepest gratitude to Dr. Carolina von Essen for originally agreeing to help and providing unceasing encouragement. It could not have been done without her.

This research has made use of the NASA Exoplanet Archive, which is operated by the California Institute of Technology, under contract with the National Aeronautics and Space Administration under the Exoplanet Exploration Program.

IRAF is distributed by the National Optical Astronomy Observatories, which are operated by the Association of Universities for Research in Astronomy, Inc., under cooperative agreement with the National Science Foundation.

This work made use of PyAstronomy, with more information and resources available at: https://github.com/sczesla/PyAstronomy

http://www.hs.uni-hamburg.de/DE/Ins/Per/Czesla/PyA/PyA/index.html.

This thesis, and all efforts that follow, are dedicated to my family.

ABSTRACT

The University of North Dakota Space Studies Internet Observatory was used to observe the transits of hot Jupiter exoplanets. Targets for this research were selected from the list of currently confirmed exoplanets using the following criteria: radius > 0.5 Rjup, discovered since 2011, orbiting stars with apparent magnitude > 13. Eleven transits were observed distributed across nine targets with the goal of performing differential photometry for parameter refinement and transit timing variation analysis if data quality allowed. Data quality was ultimately insufficient for robust parameter refinement, but tentative calculations of mid-transit times were made of three of the observed transits. Mid-transit times for WASP-103b and WASP-48b were consistent with predictions and the existing database.

CHAPTER I

INTRODUCTION

The search for life on other worlds is among the most fundamental and exciting questions that currently occupies the consciousness of our species. To that end, the robotic exploration of planets within our solar system has been underway for the better part of a century, with the Viking landers on Mars, the Cassini orbiter and Huygens probe exploring Saturn and Titan, and the future Europa Clipper mission each representing a few of the more significant contributions to the search.

The past 25 years have seen the search expand to include worlds beyond our own solar system. The discovery and initial characterization of exoplanets has bloomed into a rapidly developing field that mixes astronomy, planetary science and geology. Until recently, the variety of exoplanets being discovered were limited to large gas giant planets similar to Jupiter and Neptune. But as the precision of the instruments and refinement of methods has improved, access to planets similar in character to Earth, with qualities more favorable for habitability, has been granted.

The search for life beyond Earth is guided by looking for environments similar to those that support life on Earth. All life as we know it requires liquid water to survive and therefore the search for life both within and without the solar system is predicated on finding locations where liquid water is stable. The stability of liquid water at Earth's surface is largely attributable to the combination of Earth's distance from the Sun and the degree to which the greenhouse effect operates to keep Earth warm enough. These two

qualities conventionally define the habitable zone, which is the range of orbital distances within which liquid water would be stable on a planetary surface [075][076].

There are potentially habitable environments outside of the habitable zone of the Sun, on the moons Europa and Enceladus for example. Tidal heating caused by these moon's host planets (Jupiter and Saturn, respectively) is generating enough heat to sustain large liquid water reservoirs beneath their icy surfaces. On Earth, life can be found thriving on the deep-sea floor in environments of near-freezing temperatures and that are completely bereft of sunlight. These ecosystems are enabled by hydrothermal vents, which release heat and nutrients generated from within Earth that support the life around them. The same could be happening in Europa and Enceladus and countless other worlds beyond the habitable zones of their stars.

The habitability of Earth is the result of many factors, including the action of plate tectonics, the presence of a single large moon, a protective magnetosphere, erosion rates and chemical cycles. It is not possible to remotely sense most of these factors for exoplanets with current instruments. But the orbital distances, masses and radii are accessible, and the instruments capable of identifying exoplanet atmospheric constituents are currently being developed. Therefore, the identification of Earth-like planets in the habitable zone is possible. For example, a recent major discovery is the TRAPPIST-1 system [01] of seven planets similar in mass, radius and density to that of Earth which has at least three planets in the habitable zone of the host star. This is a landmark discovery that represents a contribution to the search for life on other worlds as significant as those made by the robotic explorers of the solar system.

CHAPTER II

HISTORY OF EXOPLANET DISCOVERY

Pulsar Timing to Radial Velocity

The first unambiguous exoplanet discoveries occurred in 1991 and were later confirmed in 1992, when two planets were detected (with a third planet being confirmed two years later in 1994) around pulsar PSR1257+12 by Alexander Wolszczan and Dale Frail using the Arecibo radio telescope [02][03][04]. These planets were indirectly detected by the pulsar timing variation (PTV) method in which regular variations in the pulsar signal caused by gravitational tugs from the orbiting planets are measured. This method also allows for the masses and periods of the disturbing planets to be determined. Despite being the first method by which the existence of an exoplanet was confirmed, it remains a novel means of detection; as of 2016, only 5 exoplanets have been discovered by pulsar timing variations and only 9 exoplanets have been found to orbit pulsars.

The first exoplanet detection around a main sequence Sun-like (spectral type G5V) star that was widely accepted occurred in 1995 and was achieved by Michel Mayor and Didier Queloz using the ELODIE spectrometer at the Observatoire de Haute-Provence (OHP) telescope in France [02][04][05]. This planet, initially called 51 Pegasus b (unofficially Bellerophon, and later dubbed “Dimidium” by the IAU in 2015), was found and measured by tracking regular Doppler shifts in the stellar absorption lines of the host star. The shifts are caused by radial motion (i.e. towards or away from an observer(of the

host star about the planet-star barycenter. By this radial velocity, or RV, method of exoplanet detection, Dimidium was found to have an orbital period of 4.23 days, a semi major axis of 0.05 AU and a minimum mass of 0.5 Jupiter masses (M_j) [05]. Later measurements confirmed that the parameters determined by Mayor and Queloz were essentially correct, and 51 Peg b served as the prototype of a class of planets known as hot Jupiters – large, gas giant planets with orbital periods on the order of days. The three exoplanets known to exist at that point - two around a pulsar and one very close to its hots star - were all equally hard to account for with contemporary models of planet formation. The inexplicability of these orbital configurations helped motivate the search for more planets and the age of exoplanets had begun.

It is worth noting that several radial velocity detections occurred before those of 51 Peg b in 1995. In particular, Latham et al. (1989) detected a 11 M_{jup} companion around HD 114762 with an 84-day period [06][07]. However, doubts in the scientific community regarding how such a large planet could form so close to its host star prevented this discovery from being celebrated. Further, uncertainty regarding the orbital inclination of the system meant that the mass estimate of $11M_{jup}$ was only a minimum, and the object could easily represent a larger brown dwarf companion instead of a giant exoplanet. These uncertainties ultimately lead to the conclusion that the object was "a probable brown dwarf" [06]. The measurements made by Latham et al. were repeated and confirmed in 1991 and again refined in 2006 [08].

Radial Velocity

Method. The radial velocity method involves observing the Doppler shift of stellar spectra as the star orbits the barycenter of a given planet-star system, red- or blue-shifting

the wavelength of the emitted starlight. The changes in wavelength can be related to the radial velocity by the following equation:

$$v_{\mathrm{r}} = \frac{\lambda_{\mathrm{obs}} - \lambda_{\mathrm{em}}}{\lambda_{\mathrm{em}}} * c \ , \tag{1}$$

where λ_{obs} and λ_{em} are the observed and emitted wavelengths, v_{r} is the radial velocity, and c is the speed of light. Spectroscopic observations of the star over time can be plotted to make a radial velocity curve, from which the curve's semi-amplitude (K) and planet's period can be directly measured. The eccentricity (e) and argument of pericenter (ω) of the orbit have distinct effects on the shape of the radial velocity curve, and can be determined by a best-fit model. The semi-amplitude (K) is related to the planet-star system by the following:

$$K = \left(\frac{2\pi G}{P}\right)^{\frac{1}{3}} \frac{M_p \sin(i)}{(M_s + M_p)^{\frac{2}{3}}} \frac{1}{\sqrt{(1-e^2)}} \ , \tag{2}$$

where G is the universal gravitational constant, P is the period, M_p and M_s are the mass of the planet and star, respectively, i is the orbital inclination with an inclination of 0º indicating a pole-on orientation, and e is the orbital eccentricity. The observables of the radial velocity method are then K, P, and e, with Ms determinable by evaluating the spectral class of the star and inferring its mass. If it is assumed that $M_p << M_s$, then $M_p \sin(i)$ can be calculated. The inclination of the orbit is not known because only the line-of-sight changes in velocity are measured by this method. The actual orbital velocity of the star about the barycenter could be greater than what is revealed by the radial velocity alone, and therefore the exoplanet's mass could be greater than what is implied.

Evolution and Limitations. The radial velocity technique of measuring distant celestial objects was already used for some decades before its first application to find extrasolar planets, particularly for the properties of single and binary star systems. The large RV semi-amplitude values on the order of hundreds of ms^{-1} were readily detectable by spectroscopic technology throughout the 1950s – 1980s, so much so that a catalog of radial velocities for 15,000 stars was available in 1953 at a precision of 750 ms^{-1} [09]. By the end of the 1970s, techniques for increasing the precision to the levels needed to detect exoplanets were being developed, including using thorium-argon (ThAr) lamps, telluric lines [010] and hydrogen fluoride gas [011] as a standard or baseline with which to measure the stellar spectrum against. These methods were capable of achieving 10 – 20 ms^{-1} precision. A notable early attempt to detect exoplanets at this precision was carried out by Campbell & Walker from 1980 - 1992 [011]. However, their small 21-star sample did not exhibit any signs of a planetary signal in that time.

In order to overcome some of the problems encountered by earlier teams, the ELODIE spectrograph was commissioned in 1993 and used optical fiber cable to feed light from both the ThAr lamp and the target star into the spectrograph simultaneously – fittingly called the "simultaneous-reference" technique. This helped eliminate sources of instrumental error, like changing air temperature, pressure and refractive index conditions overnight and between seasons, unequal slit illumination and instrument flexures that can introduce errors of tens to hundreds of ms^{-1} [012]. These advances enabled a precision of 5 – 10 ms^{-1} and the discovery of 51 Peg b in 1995. Confirmation of the first measurements of 51 Peg b was performed by a team at the Lick Observatory who achieved similar levels of precision using an iodine cell for wavelength calibration. Using an iodine cell allows

for similar corrections to those enabled by a ThAr lamp, and provides a way to track wavelength shifts caused by instrumental effects that can be subtracted from the shifts of the observed target wavelength to determine only the relative shift caused by the stellar radial motion [013].

This level of precision was maintained and incrementally built upon over the next decade and enabled several milestone exoplanet discoveries. The Lick Observatory combined radial velocity measurements taken over the course of eleven years with measurements taken by the Advanced Fiber Optic Echelle (AFOE) spectrograph (then at Whipple Observatory) to confirm the first multi-planet system with three exoplanets orbiting Upsilon Andromedae in 1999 [014]. A fourth planet was discovered around this star in 2010, yielding a system of planets with minimum masses of 0.69, 1.98, 4.13 and 1.06 M_{Jup} and orbital periods of 4.62, 241, 1,276 and 3,849 days, respectively [015]. Other milestones include making the Doppler measurements necessary to predict the first observable transit of an exoplanet: HD 209458 b was photometrically observed successfully by two independent teams in 1999 after being predicted to do so based on RV measurements [04][016].

Eventually, precisions of 3 – 5 ms^{-1} were achieved by new instruments, such as CORALIE at La Silla Observatory in Chile [017] and SOPHIE which replaced ELODIE at OHP [018]. However, a major turning point for radial velocity precision occurred in 2003, when the High Accuracy Radial velocity Planet Searcher (HARPS) instrument was installed at the European Space Agency 3.6m telescope in La Silla [019]. The HARPS instrument is capable of achieving a precision of 20 cms^{-1} from night to night and maintaining long term precision of 50 cms^{-1} [019]. These gains in precision were achieved

by several innovations that attempt to minimize all instrumental errors and maximize instrument stability, including being housed in a temperature and pressure controlled environment. The techniques employed to achieve the precision available with HARPS have become the new standard as more spectrographs are built to those specifications, and as a result, access to several new types of exoplanets, such as Neptune and super-Earth mass planets, has been granted.

The sub ms^{-1} reached by HARPS and the High Resolution Echelle Spectrometer (HIRES) at the Keck Observatory enabled the discovery of exoplanets with masses less than 25 m_{Earth} orbiting their host stars on the order of days, aptly named "hot Neptunes".

The first hot Neptunes were discovered in 2004 around stars Mu Arae, 55 Cancri, and the M dwarf GJ 436 [020][021][022] and continue to be discovered in a wide variety of planetary system arrangements. For instance, the HD 69830 system consists in three Neptune mass planets orbiting at 0.08, 0.18 and 0.62 AU and is without a gas giant planet [023]. Even more remarkable is the discovery of several "super Earth" planets, whose masses are typically less than 10 m_{Earth} [024]. While previously detected exoplanets had been gas giant planets similar to Neptune and Jupiter, planets of this type are solid, rocky bodies capable of supporting water and ice above a rocky core [024]. A notable example discovered by HARPS is the K2.5V star HD 40307, in which three super-Earth planets of minimum masses 4.2, 6.8, 9.2 m_{Earth} orbiting at 0.047, 0.081, 0.134 AU were discovered in 2009 and three more planets with minimum masses of 3.62, 3.5, 7.09 m_{Earth} orbiting at 0.24, 0.18 and 0.6 AU discovered in 2012 [025][026].

Astrophysical factors also limited the range and precision at which exoplanets could be detected via the radial velocity method. In general, radial velocity searches have been

limited to FGK and lately M spectral type stars. For stars hotter than 10,000 K (A-type and warmer), the at least partial ionization of all atoms in the star result in a continuous spectrum void of any spectral features and thus cannot be measured [012]. Further, for large A-type stars and beyond, rapid stellar rotation rates cause spectral lines to broaden and become smeared. These effects reduce how precisely the size and position of spectral features can be measured. The intrinsic faintness and mostly infrared flux for stars below 3,500 K (M-type and cooler) make them challenging to acquire the sufficient signal-to-noise ratio (SNR) needed for ground-based radial velocity measurements. Recently, however, nearby M dwarf stars that are sufficiently close to yield high enough SNR have been the targets of more radial velocity searches. This is further motivated by the stronger signals exoplanets of a given mass will produce around the lower mass M dwarf stars than around larger mass stars [012].

Other stellar phenomenon that affect all spectral types include p-mode oscillations, granulation, magnetic and other stellar activity. Turbulent convection can cause p-mode oscillations at the stellar surface, with individual amplitudes of several tens of cms^{-1} that can superimpose to create amplitudes of several ms^{-1} [012]. Granulations, or large convective cells in the stellar photosphere can create radial velocity amplitudes of several kms^{-1} across the whole stellar surface that, even when averaged out, leave jitter on the ms^{-1} level. Stellar activity, which can take the form of sunspots or bright plage regions, can create RV variations from 10 – 100 ms^{-1}, introduce short-term scatter and long-term systematic trends to data. Generally, these types of variations can be eliminated or at least greatly reduced by observations that span longer periods of time.

The combination of instrumental and astrophysical challenges discussed have presented the main limitations to current radial velocity precision. Developments in technology as well as evolving statistical methods have been used and continue to develop to wring out the last few cms^{-1} of precision for current instruments. Discoveries continue to be made as ongoing observations extend the baseline of data to analyze. Nevertheless, current technology seems to be "stuck" around the 0.7 – 1.0 ms^{-1} precision level and is hard pressed to reach the 10 cms^{-1} needed to find a true Earth-twin. Future developments include using laser combs for ultra-precise wavelength calibration, improvements in the long-term stability of instrument housing, larger telescope apertures and sensitivity from the IR to visible wavelength ranges are actively being discussed and pursued [012].

The Transit Method

Method. When the orbit of an exoplanet happens to be arranged in such a way that the planet is seen to pass in front of its host star, the occultation of the star by the planet can be used to determine certain properties of the star and planet system, including the radius ratio between the planet and star, orbital period, semi-major axis and inclination [027]. These quantities can be determined photometrically, by measuring the light emitted from a star quantified as flux and plotting the flux values over time. The resulting plot is a light curve, and photometry of this sort is common practice in astronomy for a variety of celestial objects, including asteroids, eclipsing binary and variable stars. The light curves for these objects produce distinctive shapes which are used to determine their properties (Figure 1).

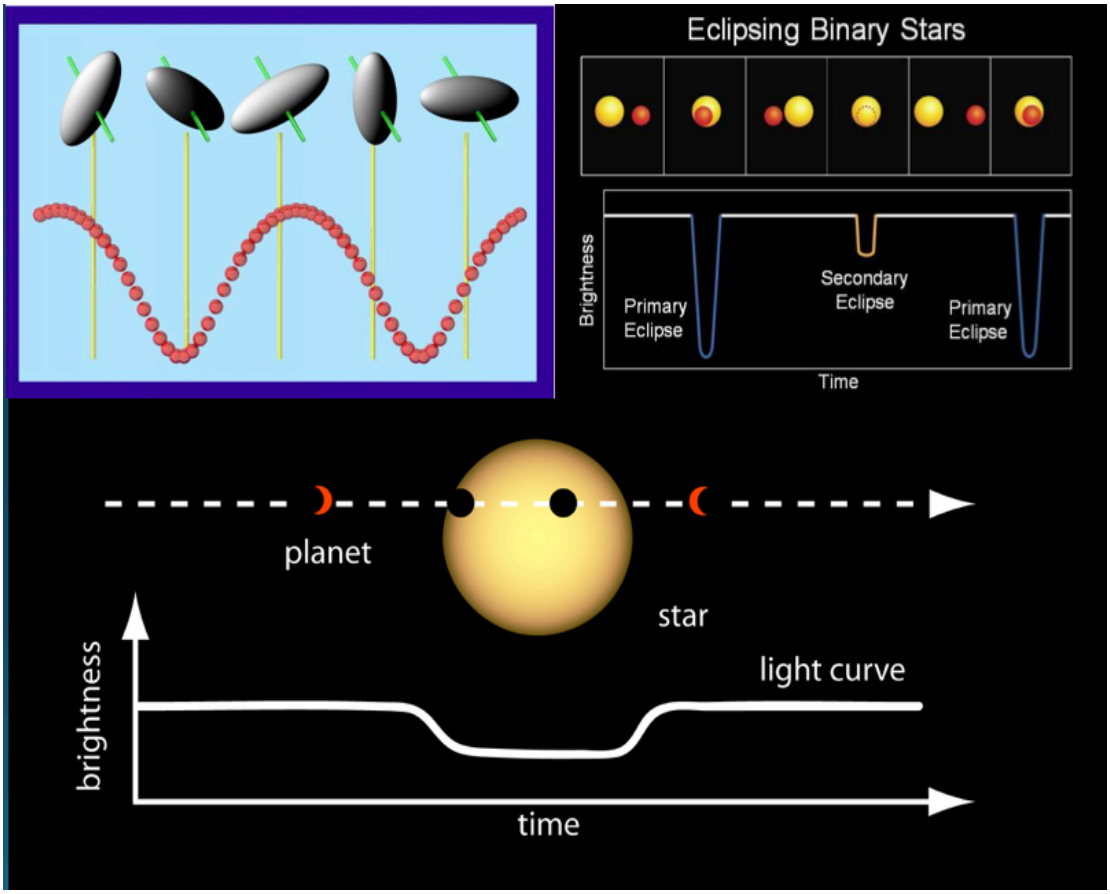

Figure 1. Representative light curves for celestial objects. Top left: Simulated light-curve of a rotating asteroid with a three-axial shaped ellipsoid model body [063]. Top right: a light curve for an eclipsing binary star system, used to measure the radii and orbital period of the stars [064]. Bottom: an exoplanet transit light curve [064].

From the light curve of an exoplanet, the radius ratio between the planet and star can be measured, and is one of a very few ways to estimate the radius of an exoplanet. The decrease in flux caused by the occultation of the exoplanet corresponds to the radius ratio by:

$$\frac{R_p^2}{R_s^2} = \Delta F, \tag{3}$$

where R_p and R_s are the radius of the planet and star, respectively and ΔF is the change in flux or transit depth (Figure 2). Estimates of the stellar radius can be made based on the

spectral class of the star and assuming the star in question is a typical member of that spectral class.

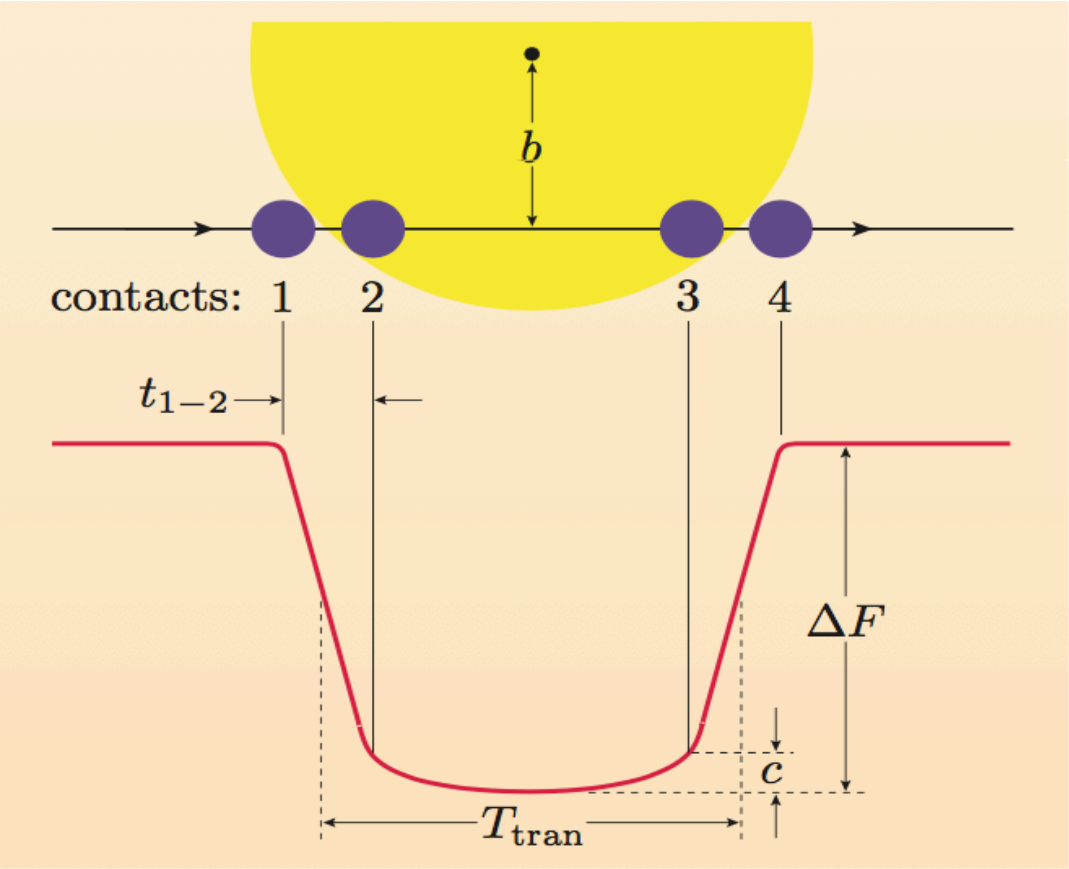

Figure 2. A schematic of an exoplanet light curve. Contact points t1 – t4, the transit depth, impact parameter b, curvature due to limb darkening c, and one measure of the transit duration T_{tran} displayed [027].

The period of the exoplanet is determined by observing consecutive transits and measuring the time elapsed in between. More precisely:

$$P = \frac{T_{elapsed}}{N_{cycles}}, \tag{4}$$

where P is the period, $T_{elapsed}$ is the time elapsed between events, and N_{cycles} is the number of cycles between the two events. In this case, N_{cycles} refers to the number of transits that have occurred. The period can be used to determine the semi-major axis of the exoplanet

orbit using Kepler's Third Law, provided an estimate for the stellar mass is available from its spectral class and assuming the planetary mass is negligibly smaller than the stellar mass.

Thus,

$$\frac{a^3}{P^2} = \frac{\left(G\left(M_S + M_p\right)\right)}{4\pi^2}, \tag{5}$$

becomes

$$a = \left(\frac{GM_S P^2}{4\pi^2}\right)^{\frac{1}{3}}, \tag{6}$$

where a is the semi-major axis, G is the gravitational constant, P is the period and M_s is the stellar mass [027].

The path that the exoplanet takes as it crosses the disc of the star is ascribed four "contact points" (Figure 2). Contact points t1 and t4 are when the disc of the exoplanet is tangent to the outside of the stellar disc crossing into and out of the disc, respectively, and contact points t2 and t3 are when the disc of the exoplanet is first tangent to the inside of the stellar disc.

The time between t1 and t2 is called the ingress and t3 and t4 the egress. The duration of the transit is typically calculated as the time between mid-ingress and mid-egress (T_{tran} in Figure 2)[027]. The transit duration can then be used with the previously described parameters to determine the orbital inclination using the following relation and assuming that $a >> R_s >> R_p$ [027] :

$$T_{dur} = \frac{P}{\pi}\left[\left(\frac{R_S}{a}\right)^2 - \cos^2 i\right]^{\frac{1}{2}}. \tag{7}$$

The shape of the light curve, particularly ΔF and the transit duration, can be related to certain properties of the planet-star system, as described above in Equations 3 - 7. Another key part of the light curve shape is the curvature of the bottom, c, between t2 and t3 (Figure 2) and corresponds to the effect of limb darkening.

Limb darkening is an optical effect where the edges or limbs of the stellar disc appear dimmer than the center (Figure 3). The severity of the limb darkening affects the severity of the curvature because the decrease in flux caused by the exoplanet is relatively greater where the star is brighter. The severity of the curvature is further impacted by the radius of the planet, the observing wavelength, and the impact parameter, *b*, which quantifies the minimum distance between the planet and stellar centers [027].

In order to account for limb darkening in transit modeling, one of several functions or laws can be used to describe the decrease in flux with increasing distance from the stellar center. Four commonly used laws are listed below:

The linear law:

$$\frac{I(\mu)}{(I(\mu=1))} = 1 - u(1-\mu). \tag{8}$$

The quadratic law:

$$\frac{I(\mu)}{(I(\mu=1))} = 1 - u_a(1-\mu) - u_b(1-\mu)^2. \tag{9}$$

The non-linear law:

$$\frac{I(\mu)}{(I(\mu=1))} = 1 - u_1\left(1-\mu^{\frac{1}{2}}\right) - u_2(1-\mu) - u_3\left(1-\mu^{\frac{3}{2}}\right) - u_4(1-\mu^2). \tag{10}$$

The 3-parameter non-linear law:

$$\frac{I(\mu)}{(I(\mu=1))} = 1 - u_2(1-\mu) - u_3\left(1-\mu^{\frac{3}{2}}\right) - u_4(1-\mu^2). \tag{11}$$

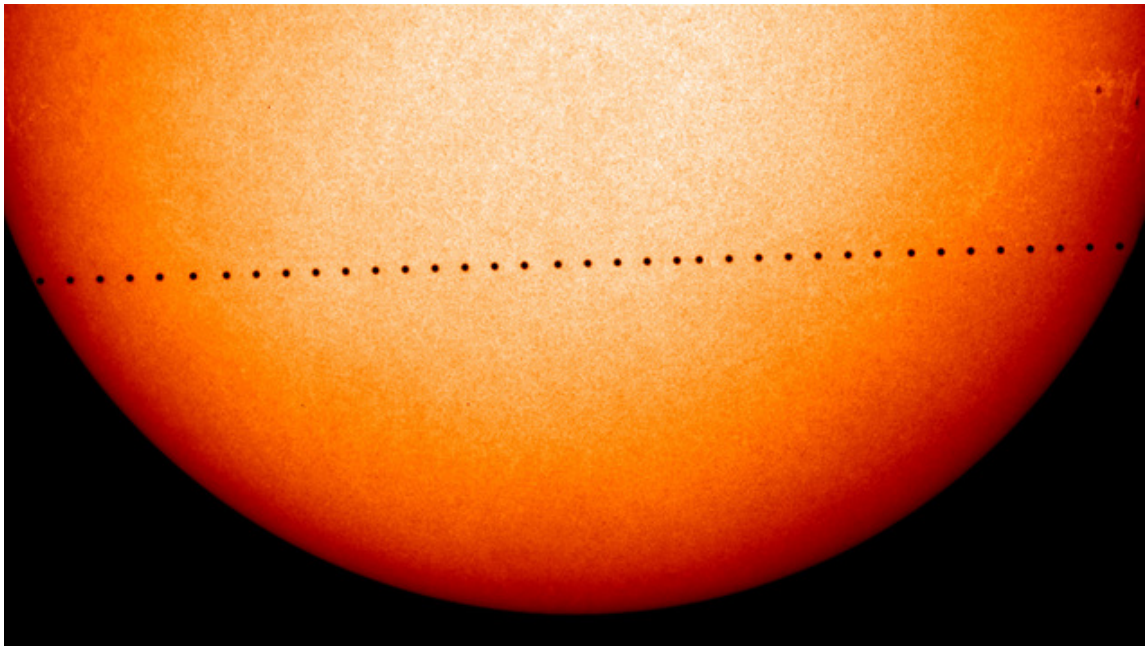

Figure 3. Time lapse image of the transit of Mercury across the disc of the Sun. The outer edge of the disc appears darker and redder than the brighter center due to limb darkening [065].

In equations 8 – 11 above, I is the intensity of light of the stellar disc, $\mu = \cos\theta$ where θ is the angle between an observer's line of sight to a point on the stellar disc and a line through the center of the stellar disc (Figure 4), u are coefficients that are either determined from interpolating stellar models of temperature, surface gravity (log(g)) and metallicity or are fitted for. The intensity is normalized to the maximum value $I(\mu = 1)$, which occurs when $\theta = 0$ and the point of observation is along the line that lead through the center of the stellar disc.

When combined with the radial velocity method, the transit method allows many key aspects of the planetary system to be revealed, including the true mass of the planet instead of a lower limit, as well as the density of the planet and thus a determination of the planet type as either a terrestrial or gas giant planet can be made. However, any exoplanet detected exclusively by the measurement of its transit cannot be confirmed as an exoplanet.

There are many celestial phenomena, particularly configurations of eclipsing binary stars and various double and triple star systems, that can mimic a transit signal and turn an exoplanetary candidate into a false positive. Therefore, subsequent observations that rule out these celestial phenomenon as the cause of the transit signal are required. These observations are most often time-intensive follow-up RV measurements to determine the mass of the candidate in question, but also include imaging the target star to resolve potential background objects and astrometric measurements. Alternatively, the developing technique of evaluating transit timing variations (TTVs) can be used to determine the mass of a transiting exoplanet candidate by use of the transit method alone.

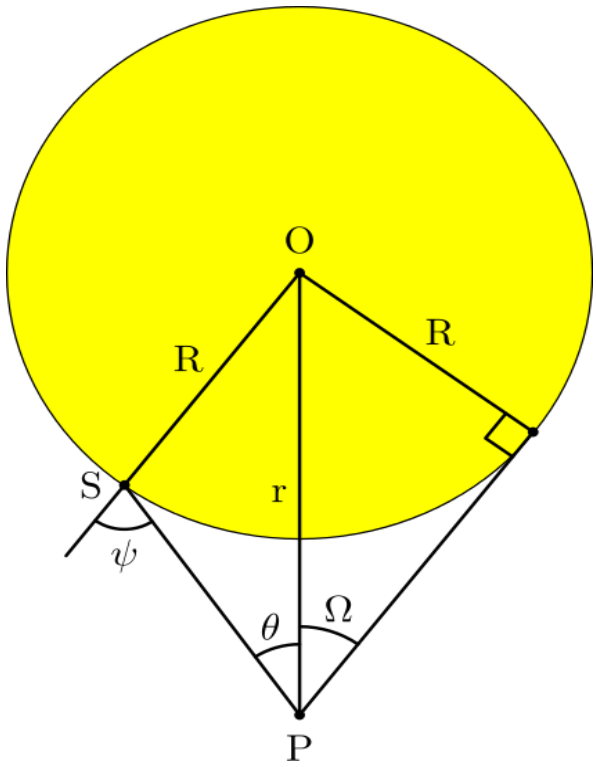

Figure 4. The geometry relevant to stellar limb darkening. Note θ is the angle between lines PO and PS, ψ is the complementary angle to θ, and Ω is the maximum angle between line PO and a line tangent to the stellar disc. The value $\cos\theta$ is used to calculate μ, used in limb darkening laws.

Evolution and Limitations. Similar to Doppler spectroscopy, the methods eventually used to photometrically measure exoplanets had previously been developed in the exploration of other celestial phenomena, like variable stars, eclipsing binaries and asteroids, and were highly dependent on the available technology. Arguably, the development of this field of astronomy that attempts to determine and compare the brightness of celestial objects (i.e. photometry) has its roots in antiquity, with one of the earliest known star catalogues compiled by Hipparchus of Nicaea in the 2nd century BCE [067]. The magnitude syntax he devised in creating the catalog was used for centuries and expanded upon past its original six magnitudes after the invention of the telescope. The development of new photometric instruments, like the Zollner visual photometer in the 19th century, necessitated the standardization of assigning stellar magnitudes to brightness determinations. The standardization protocol that was adopted was proposed by N. R. Pogson in 1856, whereby a 100x difference in brightness or intensity corresponds to a difference of five magnitudes [067]. Typically, the measurement errors of visual methods for magnitude estimation were around $^{+}_{-}$ 0.07 mag (Figure 5) [067].

Photographic plates emerged as a superior detector in the late 19th century, improving the precision of magnitude estimations to $^{+}_{-}$ 0.02 mag. Photographic plates were used as early as 1857 when George Bond observed of the double star Mizar and Alcor using the wet collodion process to take the plates [067][068]. In 1871, dry silver bromide emulsions were introduced and remained a cornerstone of photometry even during the development of photoelectric methods and until the recent development of charge coupled devices (CCD). Notable examples that highlight the power and longevity of photographic plates include the observation of several Cepheid variable stars by Henrietta Swan Leavitt

in 1907. The measurement of the Cepheid's luminosity and period contributed to the realization that the Milky Way is not the entire universe as well as the determination of the expansion rate of the Universe [067][069]. Plates were used later to perform the Palomar Observatory Sky Survey between 1950 – 1957 which was combined with other photographic surveys to create the United States Naval Observatory B1.0 catalog of over 1 billion objects in 2003 [070].

While photographic plates were widely used, the development of electronic methods was also taking place gradually into the 20th century. Electronic-based methods revolve around the ability to measure the electricity (either a voltage for photovoltaic cells or current for photoconductive cells) generated in a material when exposed to light. The power of applying these effects was aptly demonstrated by Joel Stebbins in 1910 by using a selenium-based photoconductive cell to observe the eclipsing binary star Algol to an accuracy of 0.023 mag with probable errors near 0.006 mag (Figure 6) [067][071]. The light curve produced by these observations represented the first time a secondary eclipse could be shown [067]. Until the commercialization of photomultiplier tubes (PMTs) after World War 2, photoelectric cells were used alongside photographic plates and capable of achieving high levels of photometric precision, with observers like Gerald Kron observing eclipsing binaries with probable measurement errors as low as $^{+}$- 0.002 mag in 1939 [067][072].

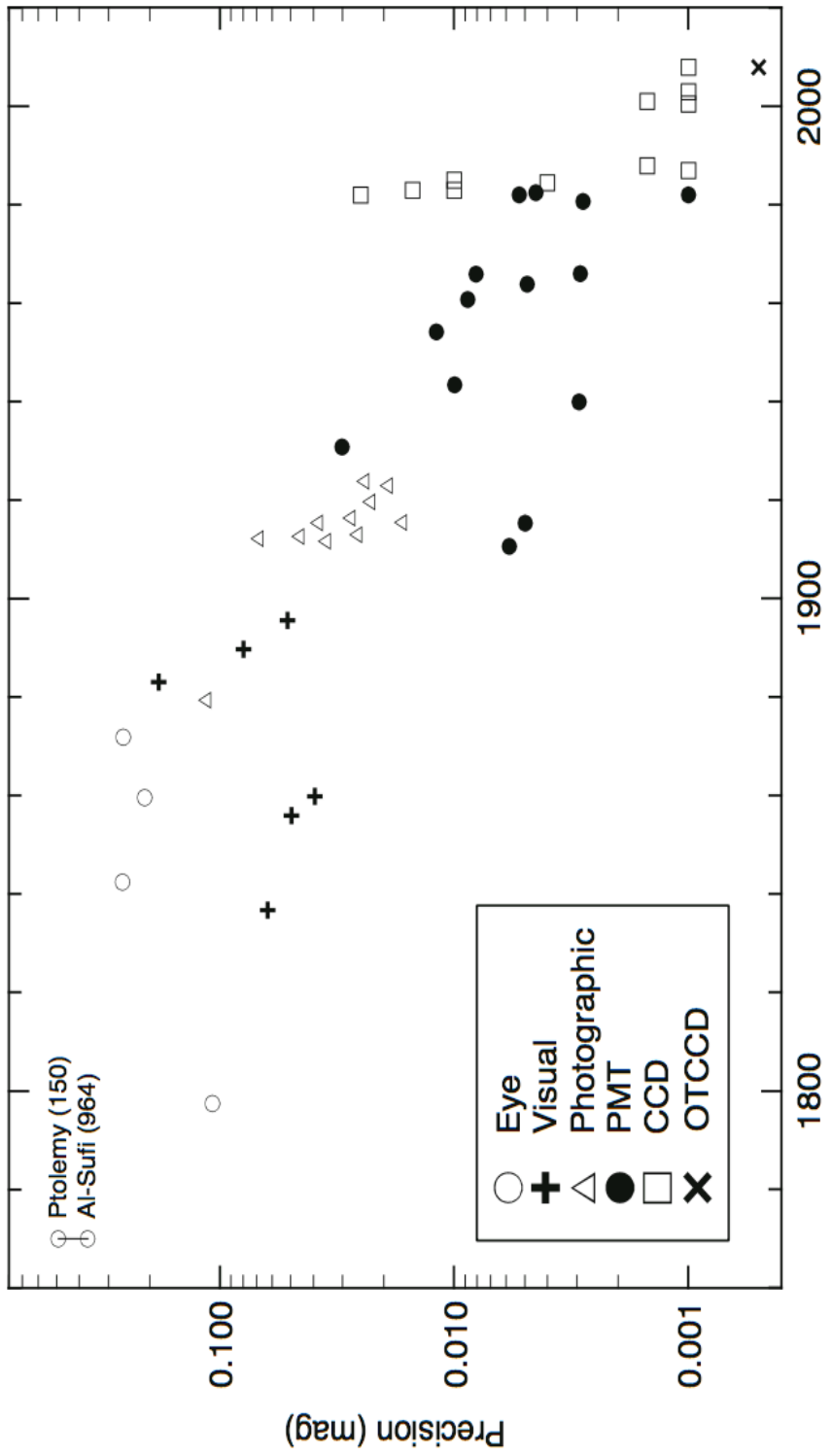

Figure 5. Approximate development of photometric precision by detector over time. "Eye" refers to those determinations done without any instrument, and "visual" refers to those determinations done with aid of an instrument like the Zollner photometer. [067]

Photomultiplier tubes operate by using a kind of cascade effect where photoelectrons are amplified in a series of increasing voltages as much as a million times. The advantages for astronomical purposes include higher quantum efficiency (13%) over photoelectric cells and the amplified photocurrent is essentially noise-free [067]. By using PMTs, in 1954 it was possible to do photometry on stars as faint as 23rd magnitude at the 200-inch Hale telescope on Mount Palomar [072]. The rise of computers and the ease provided by digitization allowed amateur astronomers to acquire and use PMTs throughout the 1970s and 80s [067].

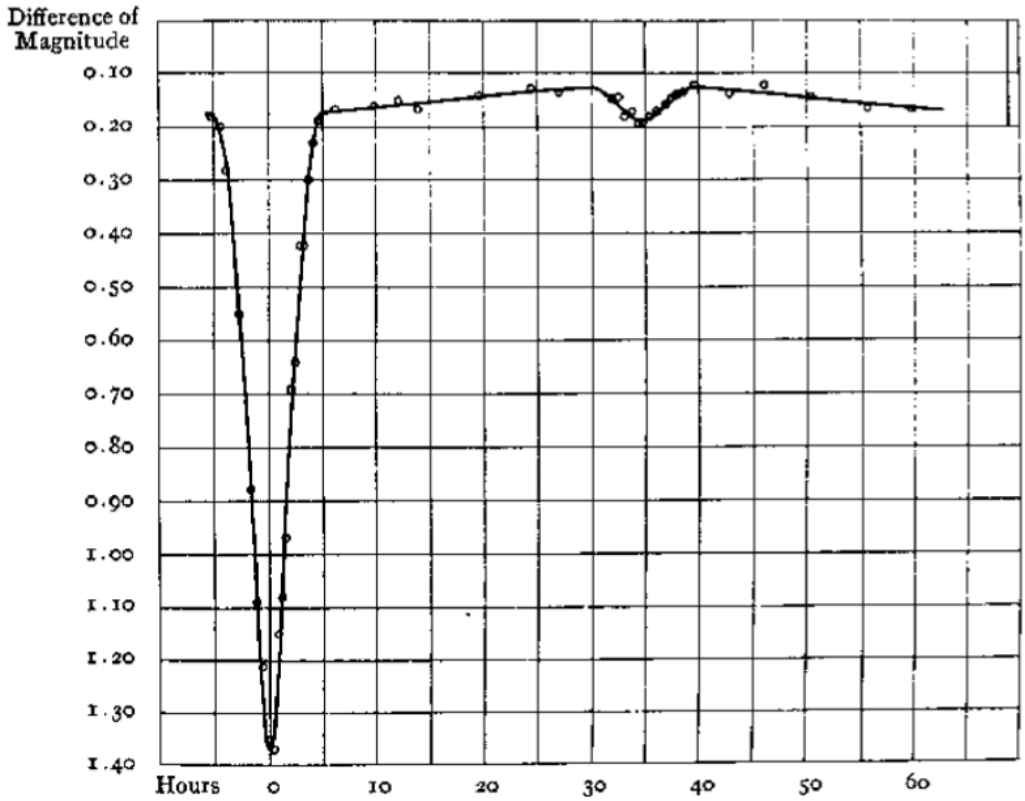

Figure 6. Light curve of eclipsing binary Algol by Stebbins (1909). The second dip or minimum at ~35 hours is the first time the phenomenon had been observed as such. [067]

The next technological breakthrough brings us to the detector used for this current thesis project as well as those used to detect the first exoplanet transits – the charge coupled

device (CCD). CCD's have a quantum efficiency upwards of 50%, reaching as high as 90% in some cases and are able of imaging a target star, comparison stars and the background sky simultaneously, which provides a huge advantage over PMTs [067] and are an essential part of differential photometry.

The planet HD 209458 b was the first exoplanet observed to transit its host star and was independently measured by two teams in 1999 using CCDs [016][028] after being predicted to transit by radial velocity measurements. The first exoplanet to be discovered by the transit method and not previously known by RV measurements was the hot Jupiter OGLE-TR-56b in 2002 [029]. The OGLE (Optical Gravitational Lensing Experiment) survey was one of several ground-based surveys, along with the SuperWASP (Wide Angle Search for Planets)[030], KELT (Kilodegree Extremely Little Telescope)[031] TrES (Trans-Atlantic Exoplanet Survey)[032], and HAT (Hungarian Automated Telescope)[033] projects that observed large swaths of the sky looking for stellar variability. These surveys were capable of achieving photometric precision between 0.015 – 0.005 mag, and enabled the discovery of additional hot Jupiter exoplanets into the new millennium. By 2009 approximately 300 exoplanets had been discovered, of which nearly 70 were transiting planets [034].

The ability to detect hot Jupiter sized exoplanets was easily within the capability of the aforementioned surveys because the change in magnitude caused by such an exoplanet is ~1%, or 0.01 mag. However, detecting an Earth-size planet orbiting its host star at 1 AU will yield a change in magnitude (i.e. transit depth) of 0.00008 mag, or ~80 ppm [073]. Ground-based photometers will be fundamentally limited from achieving such levels of

precision at least into the foreseeable future due to noise factors introduced by atmospheric effects.

One of the advantages of differential photometry is the ability to easily measure the target and nearby stars in the FOV simultaneously, which when processed, allows for the elimination of some – but not all – of the negative effects introduced by the atmosphere like scattering, spreading and reduction of the starlight before it reaches the CCD. The way the atmosphere affects starlight is also wavelength or color dependent, with bluer light being affected more than redder light.

Further, changes in the condition (e.g. humidity, temperature, aerosols) of the air column through which the telescope is looking over the course of a single evening also affect the incoming starlight and are not nearly as easily addressed, if at all, by differential photometry. Ground-based operations are also restricted in when and for how long they can observe a possible exoplanetary system due to the obvious but significant day-night cycle. The solution to these atmospheric problems that fundamentally limit the precision of photometers is to move those photometers above the atmosphere into space-borne telescopes.

After 2009, the trickle of exoplanet discoveries became a torrent, as the CoRoT space telescope and Kepler Space Telescope (KST) launched in 2004 and 2009, respectively, and heralded the transition from mere exoplanet discovery to exoplanet characterization [035]. The CoRoT space telescope was the first space telescope devoted to the detection of exoplanets and discovered the first terrestrial transiting planet in 2009, CoRoT-7b. It was the smallest exoplanet found until the announcement of Kepler-11b in 2011.

The KST had a primary mission time of approximately 3.5 years from March 2009 to October 2012 and was designed with the explicit objective of detecting transits of Earth-size planets from a large enough sample of stars in order to statistically extrapolate the population of Earth-like planets in the Milky Way [073]. The KST detector is an array of 21 CCDs for the purpose of observing a single patch of sky just off the wings of the constellation Cygnus with a FOV of 105 square degrees [074].

In order to achieve the primary objective, the CCD system was specifically designed to be able to detect the 0.008 mag transit depth of an Earth-like planet with a maximum noise limit of 0.002 mag [073] [074]. This precision was theoretically reached by estimating a photon shot and measurement noise of 0.0014 and 0.0010 mag, respectively. The photon shot noise, or Poison noise, affects all CCDs and any measurements where discrete events are counted and is determined by the square root of the number of events being counted. The measurement noise emerged in the form of readout noise in the CCD and other aspects of the instrument system.

The other key factor affecting noise measured by the KST detector was stellar variability. Noisy stars that produce relatively more sunspots or experience more frequent coronal mass ejections (CMEs) will physically change the flux of the star and inject noise in a light curve [073]. It was estimated that the stars observed by the KST would behave similarly to the Sun, exhibiting typical photometric variations of 0.000010 mag or 10 ppm at relatively infrequent intervals. It turns out that most of the stars were significantly noisier than the Sun, exhibiting much higher variability more frequently. This affected the noise accompanying the measurements made by the KST, and though the KST has enabled a vast

expansion of exoplanet science, confidence in the statistical extrapolations it was designed to enable are limited [073][074].

The failure of two of the spacecraft reaction wheels in May 2013 ended primary science operations for the KST [074]. By April 2014, analysis of the gathered data and some follow-up observations yielded a total of 3,553 discoveries, which includes exoplanet candidates and many confirmations of exoplanets previously detected [036]. As of April 2016, Kepler's haul included 1,044 confirmed exoplanets and 4,696 candidates (as listed in the KOI Cumulative table available at the NASA Exoplanet Archive) [037]. The entire exoplanet pool including non-Kepler discoveries included 1,964 confirmed exoplanets as of April 2016 [038].

Transit Timing Variations

The radial velocity and transit detection methods favor finding large exoplanets with relatively small orbits. Other planets similar in size to Earth that are relatively further away from their star in the habitable zone are thus harder to find. Indeed, conservative estimates of the number of these potentially habitable planets that have been found to date are as low as 12 and more optimistic evaluations of current findings suggest there are as many as 51 [042]. Typically, the discovery of this kind of planet has been reserved for elite, high precision instruments located in space or of otherwise limited access. However, it is possible to detect new planets previously undetected by the above methods, and even potentially habitable planets, using instruments of more modest means by observing many transits of the same planet and watching for periodic changes of when the transit occurs.

In planetary systems where one planet is seen to transit, other planets or stars influence one another gravitationally and can cause disruptions in the orbit of the transiting

planet. These disruptions can in turn change the orbital eccentricity, period, inclination or some combination of the three parameters for the transiting planet [043][044]. When this occurs, the timing, usually defined as the time of mid-transit, occurs differently than when it is predicted to occur if there were no perturbing influence. By this transit timing variation (TTV) analysis, the magnitude of the differences in transit times can be used determine the period and mass of the other non-transiting planet [043]. For example, monitoring the transit timing variations of Kepler Object of Interest 872b (KOI, or suspected but not confirmed exoplanet transit seen by the KST) enabled the confirmation of the existence of a Jupiter-mass planet exterior to an interior transiting planet, with periods of 33.6 and 57.0 days, respectively [045]. If it is the case that two or more planets have visible transits, then it is possible to determine the mass of both planets via transit observations alone, as was done for the Kepler-9 system [046] and the more recent and widely announced TRAPPIST-1 system [01].

Exoplanetary systems that are not in an orbital configuration in which periods of two planets are multiples of integers of one another (a configuration known as resonance) can exhibit timing variations on the scale of several seconds for a planet with a period of 30 days [027], a precision currently achievable only from space-borne instruments. However, if the planets in question do exhibit resonance, then the variations exerted on a large Jupiter size interior planet by some exterior perturbing planet are on the order of several minutes and is theoretically detectable from the ground [027][[044][047].

The nature of transit timing variations so far discussed which suggest a second planet requires that the variations occur in a periodic or cyclical manner. This periodicity is most readily seen in O-C (Observed – Calculated) diagrams for a given system. An O-

C diagram is a plot that visualizes the difference between when some event was observed to occur and when it was predicted or calculated to occur. For TTV analysis, the calculated values are the times at which the transit would be expected to occur if there were no perturbing influences (e.g. other planets) in the system and is represented a line normalized to y = 0 on a given O-C plot. Therefore, transits observed earlier than expected would appear as data points below the baseline, and transits observed later than expected would appear above the baseline. Several examples of O-C diagrams from KOIs (Kepler Objects of Interest) are given in Figure 7.

In some cases, the pattern of transit timing on an O-C diagram is not periodic, but instead trails downward indicating a steady decrease in the time between transits. If accurate, this could indicate that the planet is experiencing orbital decay, a process by which the planet is spiraling closer to its host star and will lead to eventual planetary destruction [048]. The evaluation of hot Jupiters that may be experiencing orbital decay is possible for ground-based astronomers by means of TTV analysis and growing in interest [049][050][051][052].

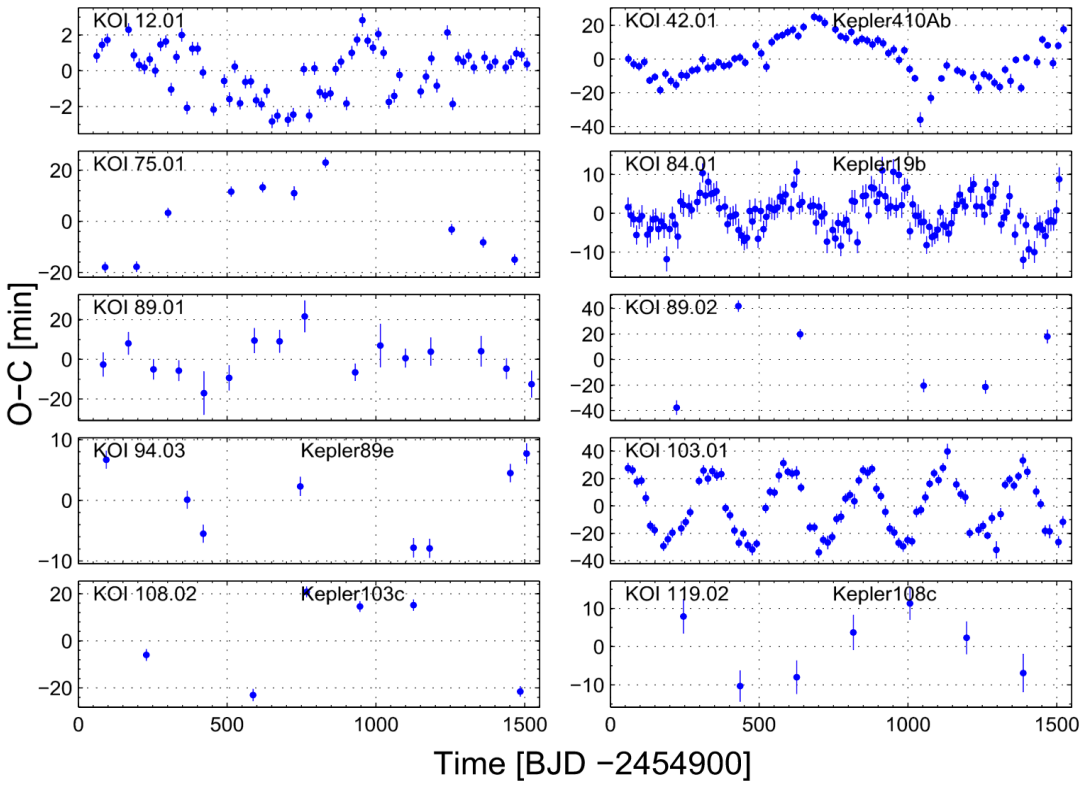

Figure 7. Several examples of O-C diagrams showing the transit timing variations. The points that are plotted represent the difference between when an event, in this case the transit, was observed and when it was predicted to be observed [045].

CHAPTER III

RESEARCH PLAN

Goals

In partial fulfillment for a master of science degree in the Department of Space Studies in the School of Aerospace Sciences at the University of North Dakota, I have observed and analyzed transits for confirmed hot Jupiter-type exoplanets using the Space Studies Internet Observatory. The goals for this thesis project are as follows:

1. Devise a target list of confirmed transiting exoplanets by evaluating the target ephemerides combined with observing site visibility from May through November 2016.
2. Perform aperture photometry on all observed transits and create light curves for each set of observations.
3. Model the new light curves to derive measurements of the target system properties, including the semi-major axis, inclination and planet-star radius ratio.
4. Combine new measurements with existing dataset for each target to refine system parameters.
5. Use light curve model to determine the time of mid-transit and combine with existing dataset to perform TTV analysis.

Aperture photometry will be performed and light curves modelled using the Image Reduction and Analysis Facility (IRAF)[1] astronomy software and the Python[2] scripting language. The transit modeling formulae created by Mandel and Agol [056] enables the measurement of the inclination, eccentricity, period, semi-major axis, planet-star radius ratio and time of mid-transit. The actual planetary radius can then be calculated if the radius of the star is known. Finally, the mid-transit time can be used with the existing dataset to infer the condition of the orbit (i.e. if the orbit is decaying), or if there is another non-transiting exoplanet present.

The execution of goals #3, #4 and #5 depend substantially on the photometric quality of acquired data. Conservatively, this data will add to the sparse datasets that exist in the literature for these targets to help refine their orbital parameters and/or aid in the development of the long baseline of observations required for a robust TTV analysis.

Observatory

The Space Studies Internet Observatory facilities includes two 16-inch (40-cm) Meade LX200 Schmidt-Cassegrain telescopes positioned on German-equatorial mounts. Internet Observatory #1 (IO1) was the primary telescope used for this research. One additional telescope, Internet Observatory #3 (IO3) was recommissioned from a state of dereliction and available for the final few weeks of observing.

The focal length of IO1 is 4227 mm, resulting in f/# = ~10. The telescope uses a Finger Lakes PL16803 CCD (charge coupled device) that is 4096 x 4096 with 9x9 micron

[1] http://iraf.noao.edu/

[2] https://www.python.org/

pixels. The field of view of this system is approximately 30 x 30 arcminutes, which represents an area on the sky about the same size as the full moon.

IO3 has a focal length of 4135 mm, also with f/# = ~10. The CCD is an Apogee U9000 with a 3056 x 3056 array of 12 x 12 micron pixels and images a FOV approximately 30 x 30 arcminutes.

Target Selection

Under the advisement Dr. Carolina von Essen (Aarhus University), a target selection strategy was devised that would maximize scientific interest with observability given the available telescope capability. Target selection began with the list of 3480 exoplanets listed as confirmed on the Extrasolar Planets Encyclopedia (exoplanets.eu) and was gradually reduced based on an initial set of criteria. These criteria were: confirmed transiting planet; a radius larger than 0.8 R_{jup}; discovered since 2012; host stars brighter than apparent magnitude of 13. The resulting list contained 95 candidate exoplanets.

Next, candidates with a declination less than -13° were eliminated because they would not be observable above the horizon or at a sufficient altitude (above 30°) at the latitude of Grand Forks (approximately 47° N). The lowest declination on the southern horizon is -43°, and 30° altitude above that corresponds to a declination of -13°. On the northern horizon, the lowest declination is +43°. Depending on the right ascension (RA) of the target, any declination above -13° could be observable, at least in theory. In practice, the ideal targets are at higher altitudes so that the atmospheric scattering of incoming light is minimized and the precision is maximized.

The resulting list of 49 transiting exoplanets was then vetted by looking at every predicted transit for all exoplanetary systems between May and November 2016 as listed

on the Exoplanet Transit Database (ETD)[3] [059] and the NASA Exoplanet Archive[4]. The observability of each individual transit event was then evaluated to see if the entire transit plus an hour before and after the start and end times would occur at sufficient altitude and darkness. The requirement for an hour before and after the transit is to ensure adequate coverage of the flux from the host star and is essential for accurate modeling. Darkness conditions and altitude were evaluated using the STARALT[5] object visibility tool hosted by the Isaac Newton Group of Telescopes [060].

The resulting list consisted of 28 transits across 9 unique targets between May and November 2016. Given the uncertainty regarding how dusk- and dawn-twilight would practically affect the night sky on any given night and throughout the season from Spring to Autumn, many of the transits could not confidently be observed with sufficient photometric quality: of the 28 transits, only 8 could be observed with confidence. As a result of the relatively small number of confident transits, the process of target selection was repeated with initial selection criteria expanded to include exoplanets with radii greater than 0.5 R_{jup} that had been discovered since 2011. The same criteria for brightness and declination were used. The final target list included 73 transit events for 18 unique targets between May and November 2016.

Operation of Charge Coupled Devices

Images taken for the purpose of transit photometry need to be calibrated to reduce noise, background flux and account for inter-pixel variations in sensitivity. These steps generally consist of applying three different types of calibration frames to the raw data,

[3] http://var2.astro.cz/ETD/
[4] http://exoplanetarchive.ipac.caltech.edu/
[5] http://catserver.ing.iac.es/staralt/

called bias frames, dark frames and flat fields. A brief description of these, including the types of issues they are intended to correct, is given below, as well as the nature of charge coupled devices in general (CCDs) and why such corrections are necessary.

Charge Coupled Devices. "Charge coupled device" is the general term for the detectors in or attached to telescopes that image, record and process incoming light that enables modern astronomers to do their science. A full discussion of the benefits and advantages of CCDs is beyond the scope of this paper, but a brief description is warranted. The first astronomical image taken with a CCD was of the planet Uranus in 1975 and the prominence of CCDs since then has grown [053]. CCDs offer a variety of advantages over previously used detectors like photo-multiplier tubes (PMTs) and photographic plates. For one, CCDs have a far greater quantum efficiency (QE, or ability of a detector to accurately turn light into electrons) than photographic plates, with modern CCDs reaching near 90% QE over the 10% QE of even the most sensitive plates [053]. Further, CCDs offer greater flexibility in observing at different wavelengths than photographic plates, meaning more types of astronomical phenomena can be successfully and easily observed.

A CCD is a flat rectangular area made up of thousands of tiny squares called pixels (from *pic*ture *el*ements), typically made of silicon but sometimes coated with other materials to change measurement capabilities of the instrument. During an exposure, starlight – or more specifically, photons - strikes each pixel and frees electrons from the silicon atoms via the photoelectric effect. These electrons would normally return to valence energy level of the silicon atom within 100 milliseconds, but are instead held in their liberated state in the conduction band by applying a voltage to each pixel to create a potential well [053]. At the end of the exposure, the accumulation of electrons ends, and

the collected charges on each pixel are then shifted along columns or rows of pixels until they are read out and converted into a digital number called a "count" that can further be scrutinized using computer software. The gain of the CCD describes the conversion rate between the number of electrons produced and the digital count value displayed (also called an analog-digital unit, or ADU). The great strength of CCDs is that they use electronics (hence the name "charge-coupled") to easily convert the analog quantity of incoming photons into a digital number. However, the electronic processing of the accumulated charges is not perfect, and neither are the pixels that make up the CCD, and so several limits exist and corrective steps need to be taken.

Saturation and Linearity. The pixels of a CCD are not capable of indefinitely collecting photons, and observations of too long an exposure or too bright an object can lead to an excess accumulation of photoelectrons. Once this limit, called the full well capacity, of a pixel has been exceeded, the pixel becomes saturated and can start to "bleed" the extra photoelectrons to other pixels on the CCD. Before this point of saturation is reached, another subtler problem occurs when the CCD enters its range of non-linearity. As mentioned above, one of the advantages of a CCD is that the flux measured by the CCD is faithfully represented by an ADU. However, as the amount of flux increases and the photoelectron accumulation approaches the pixel full well capacity, the gain or the conversion rate between the photons detected and the digital number produced will change. As a result, the image produced will no longer faithfully measure the physical phenomena being observed. It is then necessary for observers to be aware of the linearity range of their CCD in order to produce accurate science.

A second type of saturation, called A/D (for analog/digital) saturation, occurs when the gain of the CCD is not well matched to the full well capacity. If the gain is too high, then the maximum ADU value that can be calculated by the converting process will act as a ceiling and cap the values seen in the image. Photoelectrons may continue to build up in the pixel, but their representation in the CCD image will be lost [053].

Bias Frames. The electronic detector of the CCD is not sensitive exclusively to photoelectrically generated electrons, and the electronic components of the camera create electrons that show up in the pixels as noise [053]. This type of noise is inherent to the detector itself, regardless of external factors such as temperature or dust on the telescope, and are present even before an exposure begins. This noise can be corrected for by taking a zero second exposure called a "bias frame" or a "zero frame", where the camera shutter remains closed. This effectively reads out what sort of electrons are present in the pixels when no image exposure takes place. Mathematically, bias noise is corrected for simply by subtracting the pixel values measured during the zero second exposure from the pixel values of the raw images taken of the target. One bias frame is not sufficient to accurately capture the bias noise, and usually 10 or more bias frames are averaged to statistically characterize the bias noise.

Dark Frames. Additional noise inherent to the detector but largely dependent on external factors is called "dark current". This is essentially thermal noise, where warmer temperatures represent atoms and molecules that are more excited and bump into each other more frequently. These collisions create noise. For this reason, many elite observatories employ liquid nitrogen (LN_2) coolers to reduce this as much as possible and are able to eliminate dark current as a significant source of noise [053]. For those less sophisticated

(most) observatories, thermoelectric coolers are used and can reach temperatures below -30^{C}, which cannot eliminate dark current completely, and so necessitates the acquisition of dark frames [053].

A dark frame is created by taking an exposure of the same duration used for the target except with the shutter closed. In this way, the noise that has accumulated on the object frame is measured independently and can then be subtracted from the object frame to eliminate it. Like bias frames, one dark frame is not enough and so a series of dark frames are taken and averaged (or combined and pixel values are derived from the median value) to create a master dark frame.

In some cases, for exposure times that are 10+ minutes long, "scaled darks" are used instead, in which a series of dark frames with regularly varying durations (i.e. 30 seconds, 60 seconds, 90 seconds…) are taken and then scaled up to the appropriate duration length to approximate the corresponding dark current. The soundness of the approach depends on the assumption that the dark current experienced by the CCD chip is linear with time – not always the case with thermoelectric coolers [053]. For dark frames that are the same duration as the object frame, the bias noise is already included in the dark frame and it is not necessary to subtract bias from the object frame. Bias frames are still required if scaled darks are used [053].

Flat Fields. The reason flat fields are required is somewhat different than the sources of bias noise and dark current. Instead of correcting for extra electrons added to each pixel, flat fields (or just flats) correct for inter-pixel variations in sensitivity across the detector and for aspects of the entire optical system that result in uneven illumination across the detector. Some sources of uneven illumination are vignetting (in which the brightness

at the periphery of images is reduced) or dust grains on the telescope mirror or lens decreasing the flux received.

In order to account for the varying pixel responses, the ideal strategy is to image a source that can uniformly illuminate all pixels on the detector. In theory, this is simple. In practice, it is difficult. The two most popular strategies for creating flat fields are taking "dome flats" and "sky flats". Taking a dome flat consists in setting up a screen or using a special paint to draw a flat square region on the inside of the dome of the observatory, illuminating it with a relatively bright light source, and taking quick exposures. For sky flats, a section of the dusk or dawn sky is imaged several times (the ideal, most uniformly illuminated place occurring 13° from the zenith opposite the direction of the Sun). The exposure length of the flats should be such that the count values of the flat approximates the expected count value of the target exposures. Generally, this is the maximum count that can be achieved and still confidently be in the linear range of the camera.

Once attained, the series of flat field images are median combined to create a master flat. The master flat is then normalized, with some value (usually the average pixel value) assigned a new value of 1, and then divided by the (bias or dark corrected) raw images. The flats may be multiplied by the raw image frames, depending on how the processing software handles values greater and less than the average value during normalization.

The flat frames themselves also suffer from bias noise, and they too must have the bias values subtracted before calibration can occur. Further, pixel responses vary as a function of wavelength and so flat fields acquired by whatever method need to be repeated for each filter used to image the target.

Observatory in Context. The bias level for the PL16803 Finger Lakes CCD in IO1 determined from mean pixel value of the average of 20 bias frames is approximately 2243 ADU. The CCD in IO1 is cooled using thermoelectrics, and the mean pixel value at -30ºC for 20 averaged dark frames of exposures 30 and 110 seconds long are 2261 and 2314 ADU, respectively. The 16-bit CCD is capable of measuring 65,535 different ADU values (2^{16} -1), and the suggested maximum count value to stay in the linear range of the camera was 20,000.

The bias level for the Alta Apogee U9000 CCD used in IO3 is approximately 1597 ADU, and employs a thermoelectric cooler capable of reaching 40ºC below the ambient temperature. An average of thirty-one 25-second dark frames at -27ºC yield a mean pixel value of 1611 ADU. The same range of linearity was assumed for the U9000 CCD as was for the Finger Lakes CCD. These details of the telescope and CCD cameras are summarized in Table 1.

CHAPTER IV

METHODS

Observing Strategy

Predicted start, middle and end times were available for each transit identified during target selection. Ideal coverage of transits required observations to begin and end at least an hour before and after the transit. Observations were made using the Johnson Cousins R-filter (central wavelength: 634.9 nm, bandpass: 106.56 nm) and with 3x3 binning to maximize the signal-to-noise ratio (SNR). The background night sky emits more light towards the blue end of the spectrum, so the application of the R-filter helps reduces the noise introduced by the background sky and increase the flux measured from the target alone.

Twenty dusk sky flat fields were taken at the start of each evening, with twenty of each bias and dark frames also being taken if time allowed before the transit. If not, bias and dark frames were taken after transit observations ended.

Nightly observations were planned and enacted using the script-based ACP Observatory Control software platform. The flexibility and control offered by ACP scripts allows for complex observing plans spanning multiple targets, filters and exposure lengths to easily be acquired. For transit observations, however, such robustness was not needed, as the observing plan for each night was limited to a single target in a single filter with a constant exposure length for several hours.

Table 1. Details Summarizing the Telescope and Camera Capabilities of the Space Studies Internet Observatory.

Observatory	Internet Observatory 1 (IO1)	Internet Observatory 3 (IO3)
Camera	PL16803 Finger Lakes	Alta Apogee U9000
Telescope Aperture (cm)	40	40
Focal Length (mm)	4227	4135
Field of View (arcminutes)	30 x 30	30 x 30
Array Size (pixels)	4096 x 4096	3056 x 3056
Pixel size (microns)	9 x 9	12 x 12
Gain (e- / ADU)	1.4	1.2
Read Noise (e- RMS)	6.2	7.5
Bias Level (ADU)	2243	1597
Linearity Limit (ADU)	20,000	20,000

Once the sky was sufficiently dark and the target sufficiently high in the sky, several images over a range of exposure times typically from 30 to 100 seconds were taken of the target. The purpose of these exposures was twofold. First, to verify the target was in focus and near the center of the field of view (FOV) by visually pattern matching the star field to the correct star field on the Exoplanet Transit database (ETD). Second, the range of exposure times was needed to determine the maximum exposure length that remained in the linear range of the CCD camera. Selecting the proper exposure length required accounting for the changing altitude of the target over-night. The higher the altitude of the target, the less the atmosphere scatters the light and the higher the counts become. As the target becomes lower in the sky, the more the atmosphere scatters the light and the lower the counts become. The full well depth of Finger Lakes 16803 CCD camera in Internet Observatory #1 (IO1) is approximately 65,000 and the desired count for the target was 20,000 at the recommendation of Dr. Hardersen and Dr. von Essen.

Once the target was confirmed in the FOV and the proper exposure length determined, observations were made continuously and automatically throughout the evening by implementing a script in ACP. Observations were monitored throughout the night to make sure the target remained in the FOV, in focus and in the linear range of the camera.

Observing Challenges

There were several challenges that were encountered during the observing process, some of which were not realized until after the observing run was complete. One of the largest issues was the meridian flip performed by the German-Equatorial mount (GEM) used by IO1. A meridian flip occurs when a target that is being observed crosses the local

meridian from east to west in its path across the sky. The GEM operates in such a way that it cannot continuously track the target as it crosses from the eastern sky to the west, but must instead pause, wait for the target to cross the meridian, then "flip" around and re-slew to the target from the western side. This flip occurs to prevent the equipment, counterweights and cables from getting tangled up, grinding into and otherwise interfering with one another. The forced pause in observing could last up to 20 minutes and resulted in a gap in the data just as long.

Another consequence of the meridian flip is that after it occurs, the CCD chip is rotated approximately 180° relative to its orientation before the flip, resulting in the star field illuminating pixels on a completely different part of the CCD. The target not being exactly centered and the star field gradually drifting across the FOV exacerbated this consequence. Although this rotation is not an insurmountable obstacle and is theoretically accountable for by careful calibration, the variations in pixel sensitivity and other systematic changes that are introduced by this are sufficient to affect the confidence in the obtained light curves, especially if adequate calibration frames are not acquired.

For several weeks during the summer of the observing period, IO1 would be unable to plate solve, or find the correct star field with the target in it, and track it for more than a few minutes. Some nights this would prevent observing before it had started and other nights this would occur at seemingly random times after observing had already begun. In both cases, observing was unable to continue (or happen at all) for that evening and the opportunity to observe the transit was lost. The working solution for this problem was to re-synchronize the telescope to a star at the start of observing. The cause that precipitated this problem remains unknown.

Other nuisances occurred during the observing season, particularly earlier on, as the observatory operator developed his technique. These nuisances included picking exposure times that were too high and resulted in counts going non-linear as the targets altitude increased, the focus randomly jumping from image to image and grappling with several of the automated features that did not function as intended. These nuisances required a halt in observing while the problem was addressed, usually resulting in large gaps in data acquisition.

A second observatory, Internet Observatory #3 (IO3) was brought online in time for the last few weeks of the observing season. The condition of the telescope and filters was largely unknown, but many of the solutions to challenges encountered with IO1 were implemented, and three transits were observed using IO3. However, the possibility was eventually discovered that the filters in the filter wheel were improperly labeled during software configuration, and observations were made with the Clear filter instead of the R-filter.

Altogether, the obstacles and challenges encountered during the observing process were caused by a combination of the experience level of the observatory operator, atmospheric conditions and some instrumentation problems. The realization, exploration and overcoming of these obstacles have all served to educate the operator to hone his craft for superior observing going forward.

Data Reduction & Calibration

The theory and purpose behind the calibration frames (flat fields, bias and dark frames) are discussed above, and here follows the challenges and results of the data reduction using the Image Reduction and Analysis Facility (IRAF).

Images taken using IO1 experience significant vignetting, and needed to be trimmed in order to ensure proper calibration (Figure 8). All calibration frames were trimmed to the same size and combined according to their type to make master frames by taking the average pixel values of the twenty individual frames. The master flat frame was then normalized by dividing each pixel by the mean of that master flat and finally "smoothed" by fitting a second order cubic spline function to each line of the flat frame (Figure 9).

Calibration was to proceed by first subtracting the dark frames from the science frames (which included bias by being of the same exposure length as the science frames) and then applying flat field correction by dividing the dark-corrected science frames by the master flat. After several sets of data had been calibrated per the above description, it was realized that several pixel values in the science frames were negative or the calibrated science data would look far worse than the uncalibrated data. Some investigation revealed that a setting in the MaximDL camera control software provides for automatic calibration of the science frames immediately upon being taken. Despite the seeming convenience of this feature, it was at the time a setting of unknown purpose that did not have any discernible effect on the images being taken. The options for this automatic calibration could either be applying a scaled dark frame or applying a scaled dark and flat field correction.

The overall impact was that each set of data needed to be evaluated on a case by case basis to determine what calibration was needed, if any, as well as a lack of control and thus precision for the calibration process.

The final steps to prepare the data for photometry were to rotate the images on the East or West side of the meridian so the orientation of the FOV was the same and then align the images so the target is centered and in the same location from image to image. In many cases, the shift in the FOV over the course of the evening and after the meridian flip was on the order of tens and sometimes hundreds of pixels, requiring several alignment iterations if alignment was possible at all.

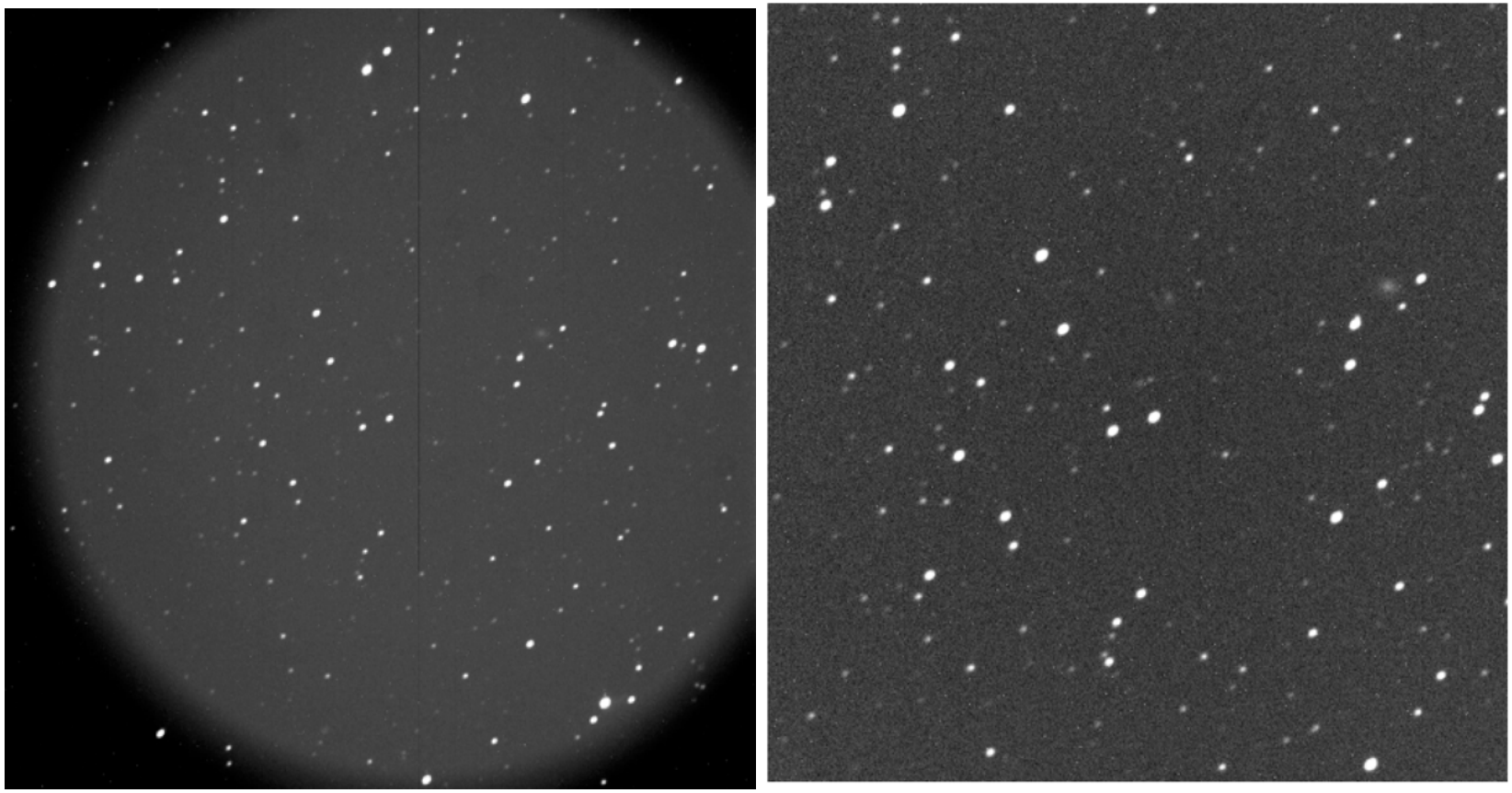

Figure 8. Comparison of full vs. trimmed frames for HAT-P-38b. Left: A full frame science image of HAT-P-38b, dimensions: 1365 x 1365. Right: A trimmed version of the same image, size 865 x 865. The dark border that "circularizes" the star field is the significant vignetting described in section 3.4.5 and 4.3. The green arrow points to the target in each image, informally the "toe of the boot" made by the four bright stars in the image center.

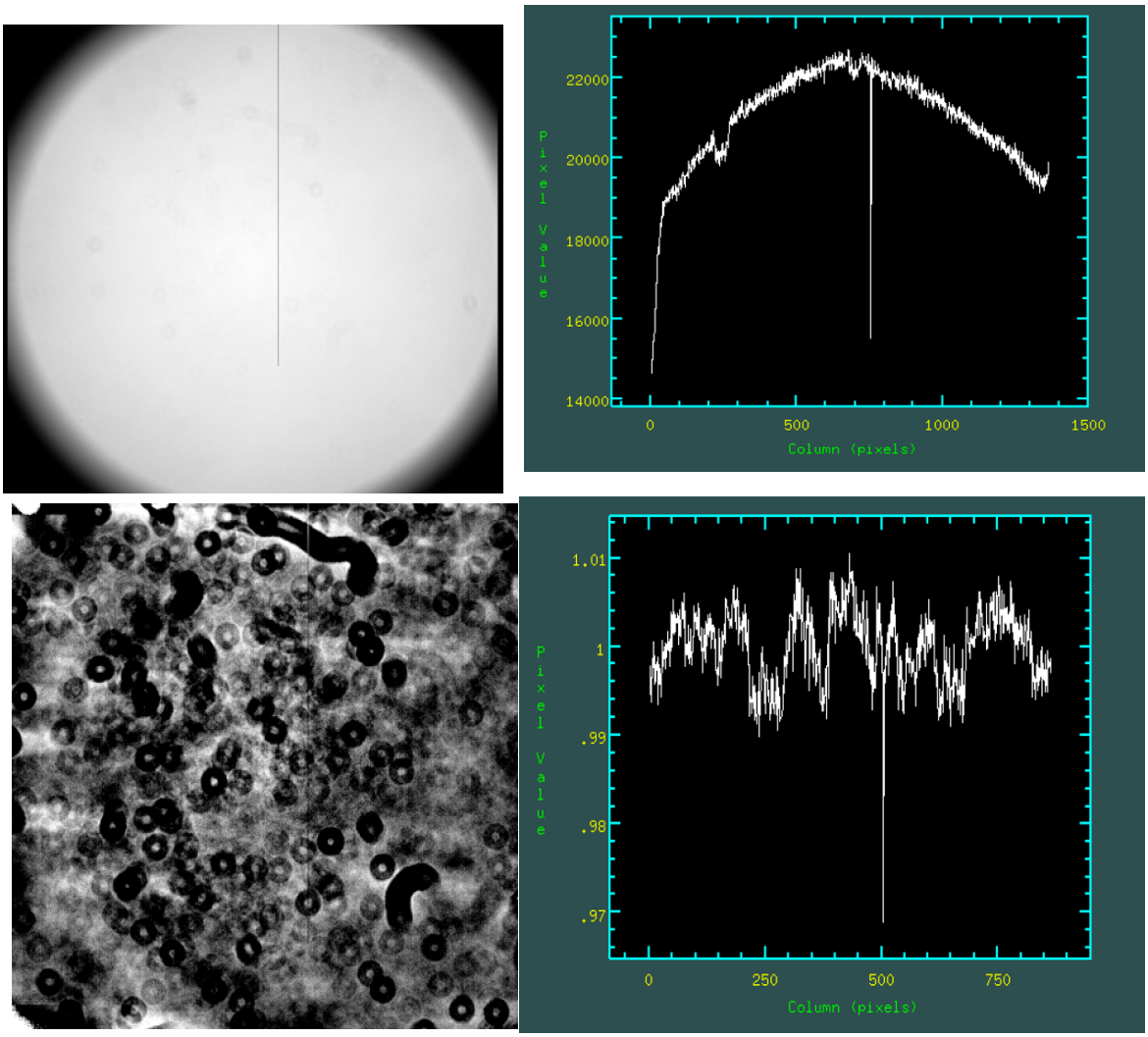

Figure 9. Flat frames before and after processing. Top Left: A full size flat field image. Top Right: A plot of pixel values along the line bisecting the image from left to right. Bottom Left: the trimmed, normalized and spline fitted flat field. Bottom Right: a plot of pixel values for the same bisecting line represented in the top right. The spike about halfway across is from a dead column of pixels, visible as a dark black line in the images.

Photometry

Differential or aperture photometry is carried out by selecting several reference stars in the same FOV as the target and dividing the target flux by one or a combination of the reference star fluxes. The goal is to eliminate systematic effects introduced by the

condition of the atmosphere (e.g. clouds, ambient temperature, humidity). To determine the flux of the target and each reference star, the background sky values need to be subtracted from the target's flux. This is measured by using an aperture around the target that is surrounded by a buffer zone and an outer ring or annulus that ideally has no stars or other astronomical features in it (Figure 10).

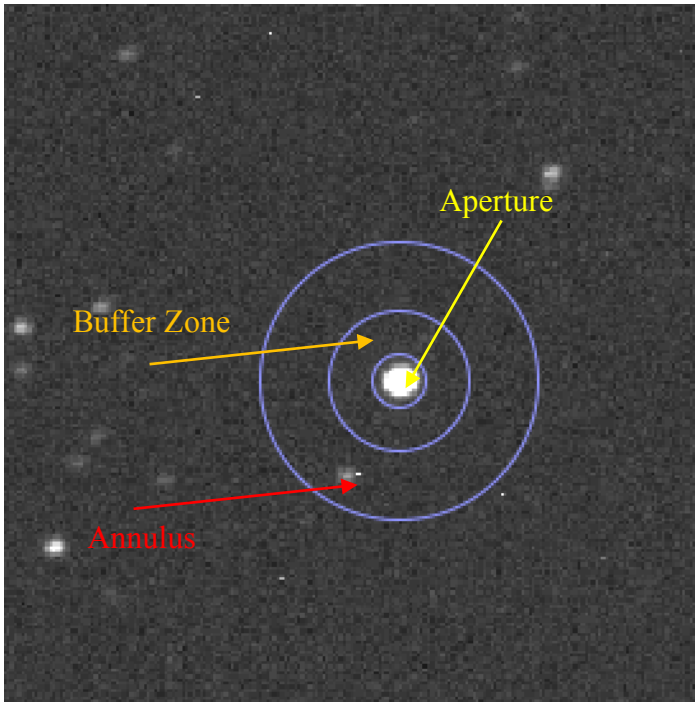

Figure 10. Aperture used for differential photometry. The aperture (yellow), buffer zone (orange) and annulus (red) used to measure target flux and sky background values.

The aperture is used to measure the total counts within its circumference, which includes flux from both the target and from the background sky. The outer annulus is used to estimate the flux from only the background sky by calculating the intensity-weighted mean of pixel values inside the annulus. The flux value from the target alone is calculated by multiplying the background sky value by the area of the aperture and subtracting that from the count inside the aperture.

For each set of data, six reference stars were selected in the FOV that had flux values close to the target's value and were as high as possible but still in the linear range of the camera, no higher than 20,000.

The ideal size of the aperture that best fits the target being measured depends on the full-width at half maximum (FWHM) of the target. The FWHM represents how spread

out the light from a target becomes as it passes through the atmosphere and strikes the CCD, and characterizes the seeing for the evening. Initially, thirteen apertures ranging from 2 – 8 pixels in radius at intervals of 0.5 were used with a buffer zone radius of 20 pixels and an annulus width of 20 pixels. Later, some data was revisited with a wider range of aperture values, ranging from 2 – 14 at intervals of 1.0. Typical values for the seeing as measured by the FWHM of the data were between 2 and 4 pixels.

The photometric measurements described above were performed using IRAF and the data for each target and reference stars were analyzed using original code written in Python, relying primarily on the numpy, scipy, and PyAstronomy[6,7] modules.

For each aperture, the sum of every combination of the six reference stars was used to calculate the relative or differential flux of the target. The differential flux was then normalized by dividing the flux values by the median flux value for the target. Outliers from this set of normalized flux values were eliminated by first fitting a third-degree polynomial to the normalized flux and identifying any data points at least two standard deviations away as outliers (Figure 11). A second and third round of outlier elimination would follow this by fitting a seven-degree polynomial to the normalized flux and identifying any data point more than 2.5 standard deviations away as an outlier. The first round uses a more conservative three-degree polynomial in order to eliminate those data points which were more extreme and more obviously attributable to a hot pixel or some such other miscellaneous instrumental error.

[6] http://www.hs.uni-hamburg.de/DE/Ins/Per/Czesla/PyA/PyA/index.html. PyAstronomy is a collection of astronomy-related Python packages for a variety of applications. It is actively being developed as of this writing (April 2017) and version 0.10.0 was used for the current research.

[7] https://github.com/sczesla/PyAstronomy

Finally, the standard deviation of the residuals, or RMS error, of the normalized flux fit to the seven-degree polynomial was calculated for each combination of reference stars. The best aperture and reference star combination was determined by identifying which aperture and reference stars produced the smallest RMS error.

Modeling

Detrending. Once the best set of aperture and reference stars is selected, the normalized flux is detrended. Detrending is necessary to remove systematic and instrumental effects that can change the overall shape of the light curve by introducing a general "tilt" or modifying the flux values at specific data points (see Figure 12, "Flux with Trend Model"). The typical factors that introduce trend into light curves are changes in airmass, "seeing" as characterized by the full-width half maximum or point spread function (PSF), the X- and Y- pixel position of the target on the CCD, and background sky values.

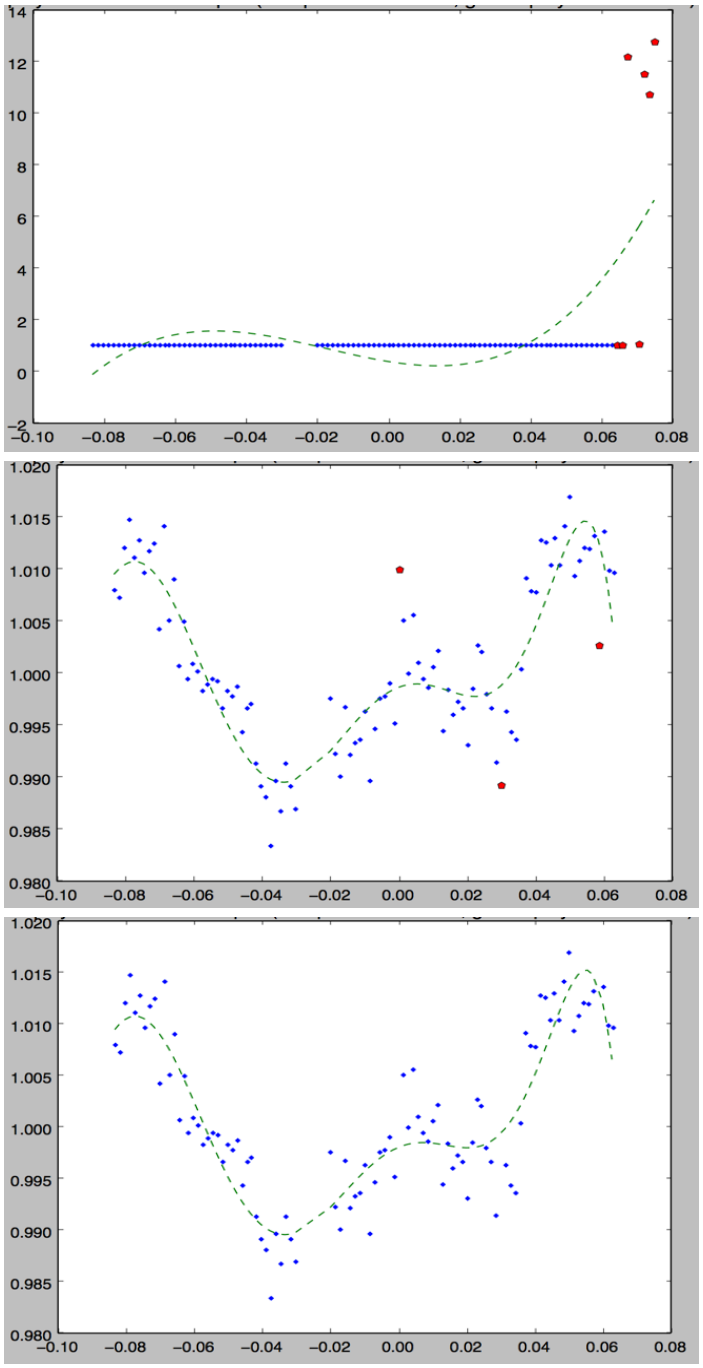

Figure 11. Example of outlier elimination for WASP-103b. Blue dots are flux values, red dots are outliers, and the dotted line is the fitted polynomial. Top: the extreme outliers eliminated using a cubic function. Middle and bottom: the second and third rounds of outlier elimination by using a seven-degree polynomial. Note by the third round, no outliers are present according to the criteria used.

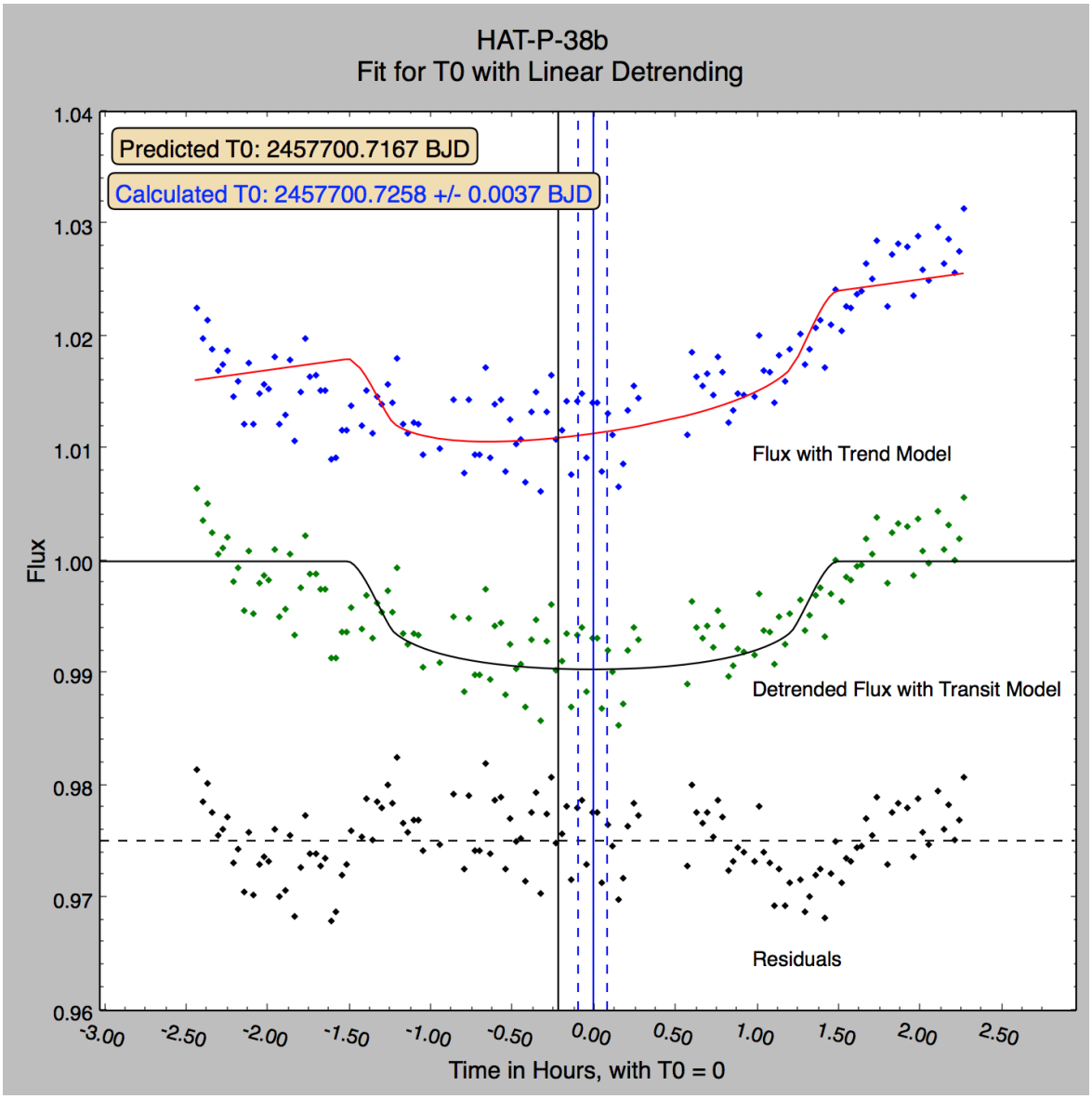

Figure 12. Time dependent detrending for HAT-P-38b. Calculated mid-transit time, T0 (blue line), with one-sigma errors (blue dotted lines) and predicted mid-transit time (black line). Top: Normalized flux with trend model. Middle: Detrended flux with transit model. Bottom: residuals.

Two detrending approaches were explored, loosely following the method of von Essen et al. (2016) [052]. The first option is to detrend the normalized flux according to a linear combination of the systematic factors described above which can be measured for each image in a set of data. The second option is to detrend using a time-dependent

quadratic equation that cannot be traced back to a real physical quantity. Though somewhat lacking in conceptual justification, the time-dependent quadratic detrending function is effective and widely used, including by the SuperWASP exoplanet transit survey [027].

To determine whether systematic or time-dependent detrending was appropriate, both detrending methods were performed and the best combination of parameters within each method also needed to be found, as not all parameters are always needed to get the best fit. The parameters combined for the systematic detrending were the X- and Y-center position of the target, air mass, PSF and sky background. The time-dependent detrending function consists of a linear and quadratic coefficient. Both methods also include an "offset" parameter used to align the detrending function with the normalized flux on the y-axis and had typical values around 1. A trend model was constructed using each combination of these parameters and then fit to the normalized flux. The goodness-of-fit for each combination of parameters was determined by using a least-squares fit of the detrended flux to a transit model and compared by calculating the chi-square value, Bayesian Information Criterion (BIC) and the RMS error.

The BIC value determines the appropriateness of a model and set of parameters used to fit a given set of data and in this case was calculated by [054]:

$$BIC = \chi^2 + k \cdot \ln(n), \tag{12}$$

where X^2 is the chi-square value, k is the number of free parameters, and n is the number of data points or observations. The utility of the BIC is in addressing the fact that a model with more free parameters may provide a better fit for the data but is at risk of over-fitting. John von Neumann said, "With four parameters I can fit an elephant – and with five, make him wiggle his trunk" [055], indicating that the more free parameters that are used to fit a

set of data, the more likely it is to be a better fit, regardless of the appropriateness of the parameters used. The BIC penalizes a model with more parameters and thus the model that fits the data with a lower BIC value should be selected. The BIC in this case is particularly useful for selecting between trend models made from possible combinations of the systematic parameters.

The BIC, chi-square and RMS error values were calculated for each combination of parameters. The three values were compared for each combination by normalizing the values to the minimum value of that criteria and summing the normalized BIC, chi-square and RMS error values. For example, if a particular combination of parameters had a normalized sum of 3.0, that would indicate that each BIC, chi-square and RMS error value associated with it was the lowest of all the combinations. Once the best set of detrending parameters were selected, their coefficients in the detrending function were fitted for using Markov Chain Monte Carlo (MCMC) modeling with initial values of the coefficients set to the values derived from the least-squares fit.

Transit Fitting. Exoplanet transits were fitted by implementing the formulae developed by Mandel and Agol (2002) [056]. Their model uses the parameters listed in Table 2 and can be adapted to accommodate linear, quadratic and non-linear limb darkening models as well as circular or keplerian orbits. Transit models using quadratic limb darkening for circular orbits were used for this research. Quadratic limb darkening models are adequate and widely used [045] and the assumption of a circular orbit is consistent with typical orbits of hot Jupiter exoplanets [057]. Limb darkening coefficients were interpolated from Claret (2000) [058]. The Mandel and Agol (2002) formulae were implemented using Python. For the purposes of fitting for the time of mid-transit, all times

were converted from Julian date (JD) to barycentric Julian date (BJD) using the method and code devised by Eastman et al. (2010) [062][8].

Further, it was assumed that transit midpoint was actually recorded during observing and the first and last exposure timestamps were used to limit the range of possible values for the mid-transit time. Initially, the mid-transit time was set to the exposure timestamp that was exactly in the middle of the observing run. This convention was easier to implement generally for different targets, but as will be discussed, was not always the soundest of assumptions.

Mid-transit times were fitted for using the same procedure as for the detrending function coefficients, namely MCMC fitting with initial values set by a least-squares fit. Errors given are the standard deviation of the MCMC fitting.

[8] http://astroutils.astronomy.ohio-state.edu/time/

Table 2. Name and Description of Parameters Used in Mandel Agol (2002) Transit Modeling [056]. These Parameters are for a Model that uses Quadratic Limb Darkening and Assumes a Circular Planetary Orbit.

Mandel Agol (2002) Transit Model Parameters	
Parameter	**Description**
Planetary radius ratio	The ratio of the planetary radius to the stellar radius
Semi-major axis (stellar radii)	The average orbital distance of the planet from the star in units of the host star's radius.
Inclination	Inclination of the planetary orbit relative to observer. 90 degrees would be perfectly edge-on.
Orbital period (days)	The time it takes for the planet to complete one orbit around the host star, in Earth standard days (24 hours)
Linear limb darkening coefficient	In the quadratic function describing the decrease in stellar brightness from the center of the disc towards its edge, or limb, the coefficient of the linear component.
Quadratic limb darkening coefficient	In the quadratic function describing the decrease in stellar brightness from the center of the disc towards its edge, or limb, the coefficient of the quadratic component.
Stellar companion flux ratio, b	Describes the flux ratio between a stellar companion and main star. Applicable for binary stars, defined as b = 0 for this research.

CHAPTER V

RESULTS

At the conclusion of the observing run that lasted from May to November 2016, eleven transits for nine unique targets had been observed out of the seventy-three that were identified. The system parameters for the nine unique targets are given in Table 3. Once the detrending was implemented either by systematic factors or a time-dependent function (or both in separate analyses), it was realized that the data quality was not suitable to perform a robust parameter determination and of limited use for transit timing variation analysis. The challenges encountered during the observing process, particularly the meridian flip, unexpected and inadequate auto-calibration, and insufficient transit coverage contributed to the difficulty in obtaining high quality data.

Since the quality of the data is not sufficient to fit for the transit parameters, goals #3 and #4 could not be met. The next best option was to fix the values of the transit parameters to the accepted values in the available literature, and fit only for the time of mid-transit. This would allow for a conservative TTV analysis tentatively meeting goal #5. Presented and discussed here are the four most interesting transits, either being of the highest relative quality (WASP-103b and WASP-48b) or demonstrating key lessons learned (HAT-P-16b and HAT-P-38b). The mid-transit times were then compared to the existing datasets available on ETD and assessed qualitatively as to whether the results of this research matched or were inconsistent with any apparent trend. A summary of the mid-

ttransit times that were calculated either by time-dependent or systematic detrending is given in Tables 4, 5 and 6.

The ETD offers a publicly available model-fitting procedure where astronomers can upload a simple text file with flux or mag values, errors, and time in either geocentric or heliocentric Julian date formats, apply a time-dependent linear or quadratic detrending function, and fit for the parameters used in the Mandel Agol [056] formulae using a linear limb darkening law. It is a simple, easy to use interface that conveniently plots data input by the user on the O-C diagram with other observations of the target that have been submitted to the database. Initially, ETD was used in this way to compare the results of their publicly available model-fitting of the mid-transit time to the mid-transit time calculated for this research using Python and also to plot the data of this thesis on the available O-C diagram.

However, this approach was abandoned in part when a discrepancy was noticed between HJD times reported in different locations on ETD. For example, the mid-transit time in UT reported for HAT-P-38b on November 8, 2016 was 05:03 UT. Converting this value to JD time yields 2457700.7104 JD, or 2457700.7159 HJD. The predicted mid-transit time given during the model-fit procedure was 2457700.7110 HJD, which aligns much closer to the JD time than the HJD calculated elsewhere. This discrepancy was observed for all of the transits and predicted mid-transit times and undermined the confidence that could be placed in how ETD added data from this research to its currently existing O-C plots. Therefore, the O-C plots on ETD are still used, but data from this research is added manually by adding a five-pointed blue star approximately where the mid-transit time calculated using Python would be. Figure 5.2 shows the how the observed

discrepancy on ETD exaggerates the placement of the calculated mid-transit value. If nothing else, this serves as a valuable lesson in time-keeping and not putting blind faith in online resources.

The results of the calculation of mid-transit times for each of the four datasets are presented so that the normalized flux with the trend model, detrended flux and transit model fit for mid-transit time, and the residuals of the detrended flux and transit model are shown on the same set of axes. The normalized flux with trend model and the residuals are offset by an arbitrary amount but kept on the same scale for ease of interpretation. For each figure, the black line represents the predicted mid-transit time, the solid blue line represents the calculated mid-transit time and blue dotted lines represent the 1-σ uncertainty in the calculated mid-transit times as determined from the standard deviation of the MCMC fit.

Table 3. System Parameters of Targets for which Transits were Observed. Note that Planetary Radius is Presented in Units of Jupiter Radii for Convenience, which is Different than the Quantity used in the Mandel Agol Transit Model. Level of Uncertainty for Semi-Major Axis Values are Denoted by Parentheses around Last Significant Digit. Estimates of Stellar Radius were the Limiting Factor Regarding Precision. Values taken from the Exoplanet Encyclopedia [066].

Planet Name	Planetary Radius (R_{Jup})	Semi-major axis (stellar radii)	Inclination	Orbital Period (Days)	Apparent Magnitude	Transit Depth (mag)	Transit Duration (minutes)
HAT-P-38 b	0.825	12.18(8)	88.3	4.640382	12.56	0.0097	182.45
WASP-103 b	1.528	2.97(3)	86.3	0.925542	12	0.0129	155.58
WASP-48 b	1.67	4.2(3)	80.09	2.143634	11.06	0.0108	191.08
HAT-P-16 b	1.289	7.18(1)	86.6	2.77956	10.8	0.0101	184
HAT-P-53 b	1.318	5.62(0)	86.2	1.9616	13.73	0.0135	128.07
HAT-P-57 b	1.413	5.8(2)	88.26	2.465295	10.47	0.0102	209.9
TrES-3b	1.305	5.97(9)	82.15	1.306	12.4	0.0291	77.4
WASP-52 b	1.27	7.4(0)	85.35	1.7497798	12	0.029	108.58
KELT-1 b	1.116	3.61(4)	87.6	1.217514	10.7	0.0066	153.245

Table 4. Summary of Mid-Transit Times, Predicted and Calculated, for HAT-P-38b. The Various Labels Under the "Calculated" Column Describe the Type of Detrending that was Performed. In this Case, "All" Refers to X-/Y-Center Position, Airmass, Sky Background and PSF.

HAT-P-38b	
Predicted T0	2457700.7167
Calculated T0's:	
Time Dependent - Linear	2457700.7258 +/- 0.0037
Systematic – All	2457700.726 +/- 0.0030
Systematic – Sky Background	2457700.7205 +/- 0.0037

Table 5. Summary of Mid-Transit Times, Predicted and Calculated, for WASP-103b. The Various Labels Under the "Calculated" Column Describe the Type of Detrending that was Performed. In this Case, "Systematic - Best" Refers to X-Center Position, Airmass, Sky Background and PSF.

WASP-103b	
Predicted T0	2457525.8298
Calculated T0's:	
Time Dependent – Linear	2457525.8290 +/- 0.0010
Systematic – Best	2457525.8300 +/- 0.0010

Table 6. Summary of Mid-Transit Times, Predicted and Calculated, for WASP-48b. The Various Labels Under the "Calculated" Column Describe the Type of Detrending that was Performed. In this Case, "Systematic - Best" Refers to X-Center Position, Airmass, and PSF.

WASP-48b	
Predicted T0	2457606.7933
Calculated T0's:	
Systematic – Best	2457606.7935 +/- 0.0013
Time Dependent – Linear	2457606.8008 +/- 0.0020

HAT-P-38b

Exposures for HAT-P-38b were 100 seconds long, cooled to -30º C and, being one of a few sets of data taken after the auto-calibration was realized and deactivated, this dataset was suitable for both bias and flat correction. A meridian flip occurred at 05:32 UT during observing and resulted in a gap in data acquisition approximately 20 minutes long.

Besides this gap, transit coverage is assumed to be complete. Observing began at 02:50:16 UT on November 8, 2016 and concluded at 07:32:18 UT. Predicted transit start, middle and end times are 03:32 UT, 05:03 UT, and 6:34 UT, respectively.

The fitting procedure and analysis of mid-transit time yielded ambiguous results for HAT-P-38b. The predicted mid-transit time for the transit was 2457700.7167 BJD. At first, the ideal detrending function was identified to be a linear time dependent model, and the time of mid-transit was calculated to be 2457700.7258 +/- 0.0037 BJD. This corresponds to a difference of approximately 13 minutes late (+/- 5.3 minutes) (Figure 12). Despite considerable scatter in the most recent observations logged on ETD, all transits listed on ETD occur earlier than predicted (below the grey dotted line) (Figure 13).

This dataset was further explored by detrending and fitting according to the best set of systematic parameters (background sky) (Figure 14) as well as the full set of systematic detrending parameters (X-/Y-center, PSF, airmass, background sky) (Figure 15). The calculated mid-transit times were 2457700.7205 +/- 0.0037 and 2457700.726 +/- 0.003, respectively. The mid-transit time determined by detrending only by the background sky value is not consistent with either the predicted mid-transit time or the mid-transit time calculated using linear detrending. Being identified as the "best" systematic detrending parameter probably resulted from the bias towards fewer parameters that using the BIC value introduces. However, the mid-transit time calculated using all of the systematic detrending parameters agrees nicely with the linearly detrended value, and lends credibility to the utility of using the time-dependent detrending methods.

The trend such as it is on ETD indicates that the transit is occurring earlier than predicted, as much as 28 minutes in some cases. In the event that this is an accurate

indication of possible orbital decay, and the transit did indeed occur close to half an hour sooner than anticipated, observations on November 8 would still have full coverage of the transit, albeit with shorter pre-ingress coverage. In other explorations of the data, in which detrending and mid-transit time fitting were performed simultaneously instead of in separate sequential steps, several combinations of systematic detrending parameters yielded mid-transit times earlier than the predicted value. The range of mid-transit times that were calculated in this way with different combinations of systematic detrending parameters and the mid-transit time simultaneously are depicted in Figure 16. They are sorted from lowest (earliest) to highest (latest) and so far as could be discerned, there was no connection between the parameters used and whether the calculated mid-transit time occurred at an earlier or later time.

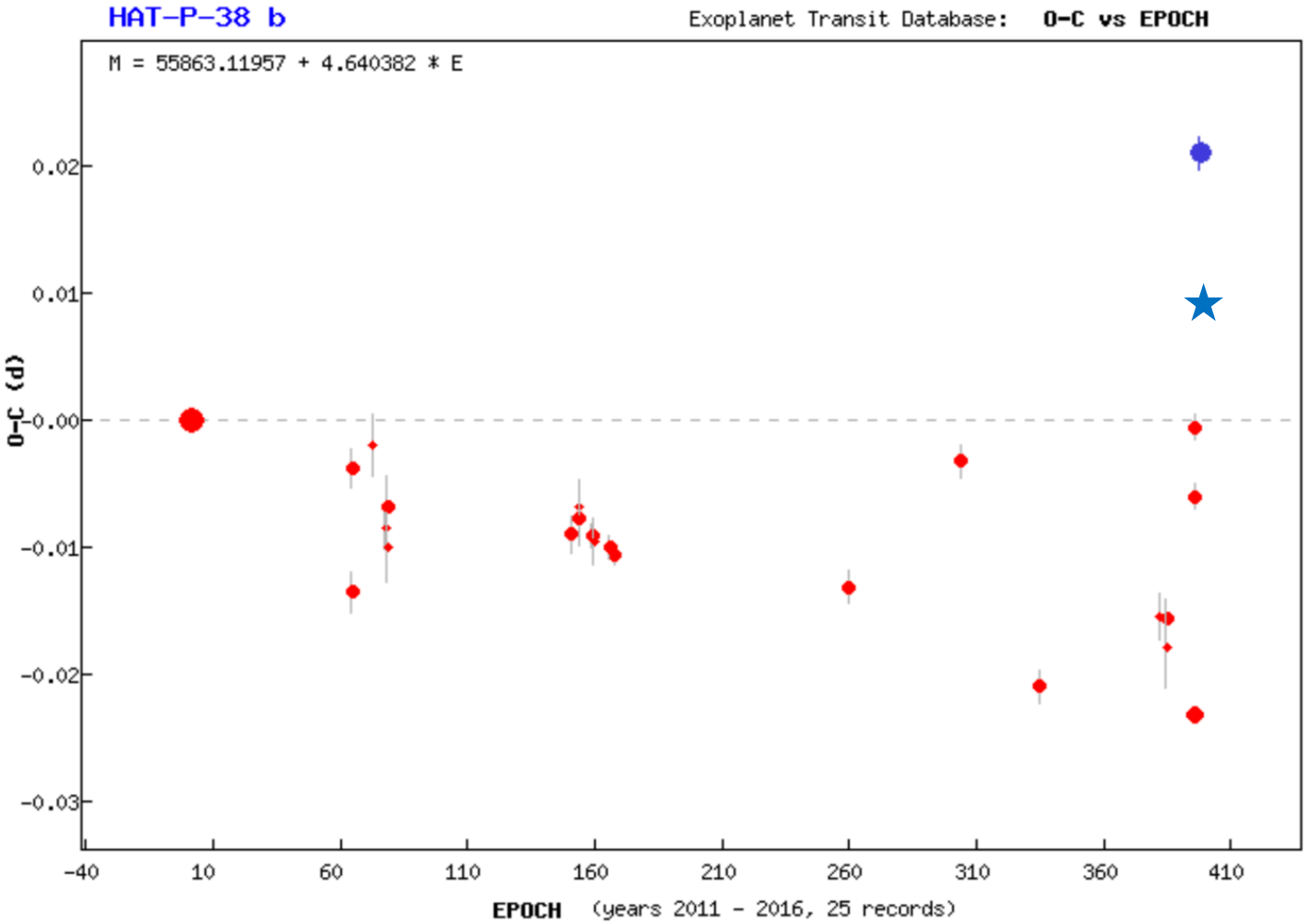

Figure 13. O-C diagram for HAT-P-38b available on ETD. Red dots represent existing data contributed by other observers. The blue dot is when the modeling service available on ETD calculated the mid-transit time, the blue star is the mid-transit time calculated by modeling independent of ETD [059].

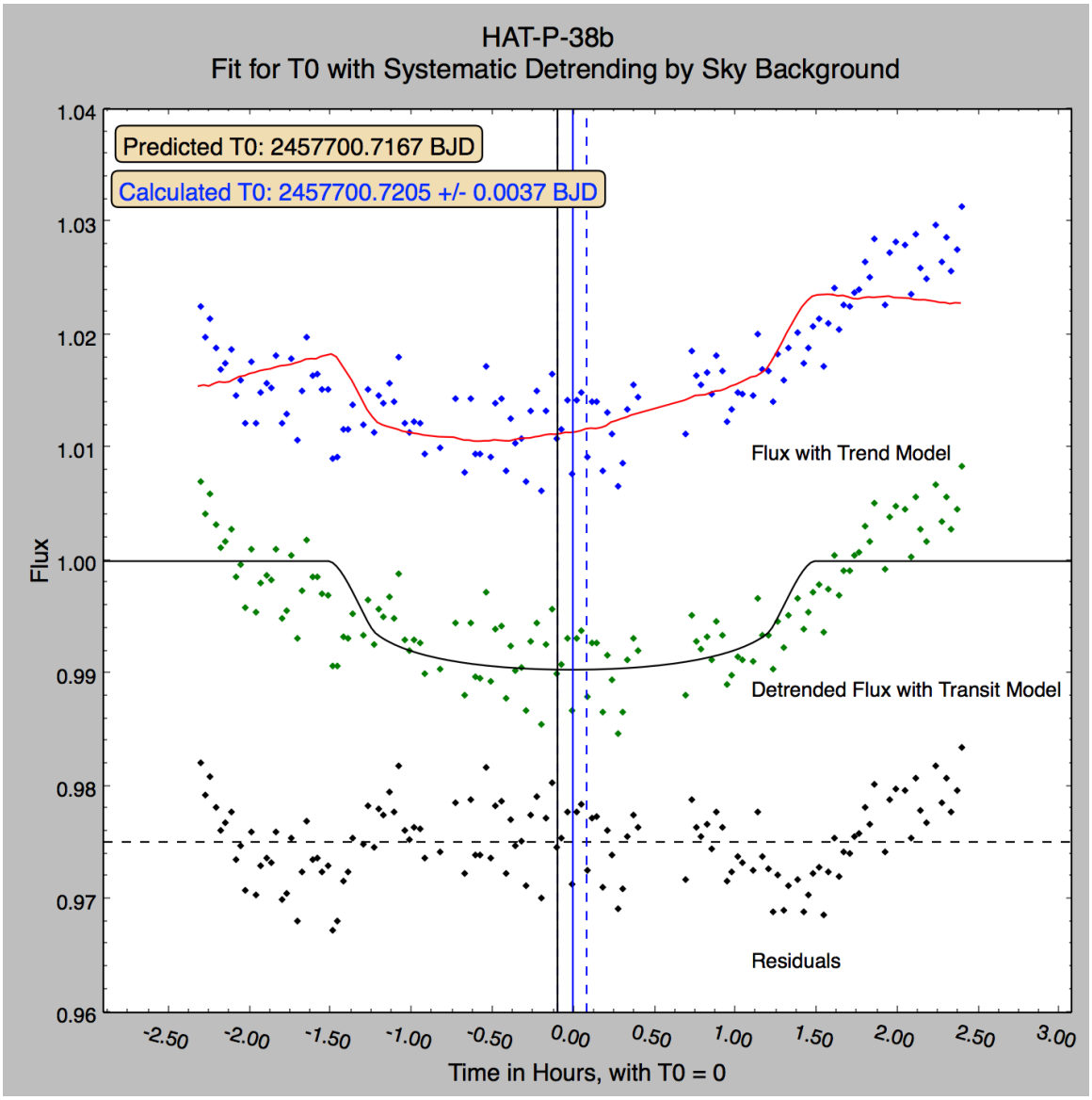

Figure 14. A transit model fit for mid-transit time of HAT-P-38b using the best set of detrending parameters. That was singularly the sky background counts. The predicted mid-transit time (black line) is just outside the one sigma error range (blue dotted lines) for the calculated mid-transit time (solid blue line).

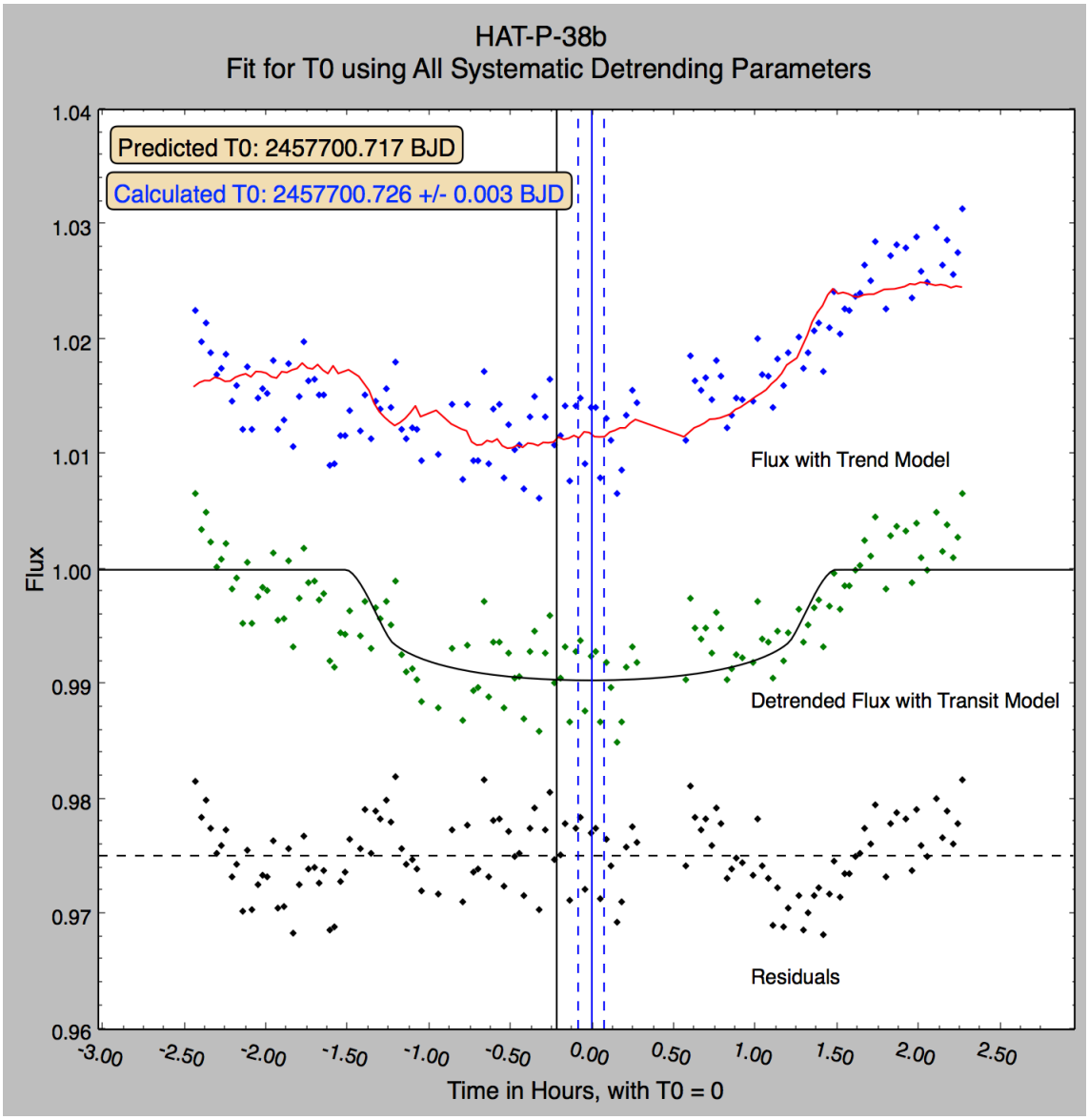

Figure 15. Transit model fit for mid-transit time of HAT-P-38b using all of the systematic detrending parameters. Those are X-/Y-center, airmass, PSF, sky background.

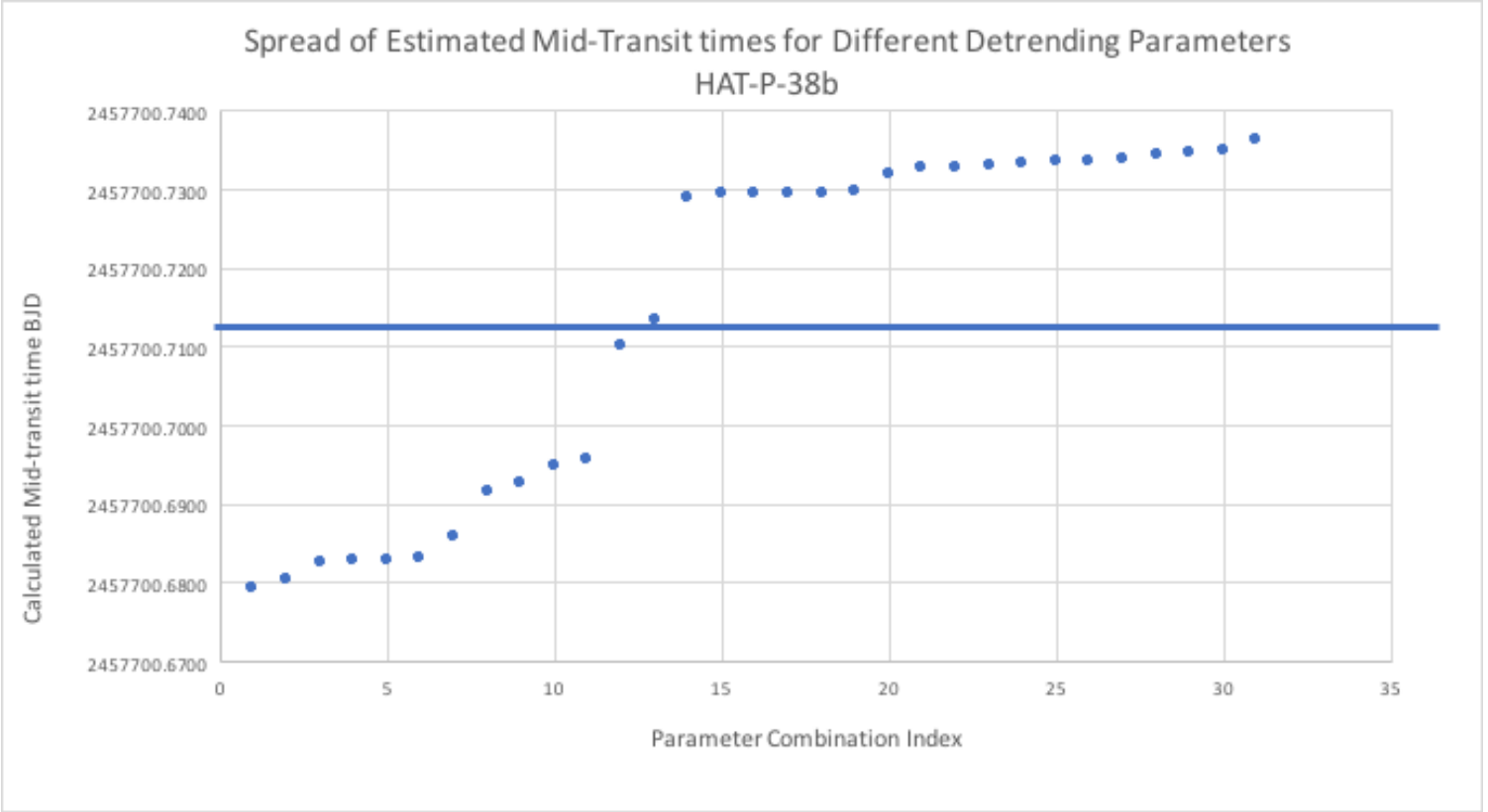

Figure 16. The calculated mid-transit times for all 32 combinations of systematic detrending parameters fit simultaneously with the mid-transit time for HAT-P-38b. It appears as if there are two general pockets of time that are calculated, between 2457700.68-69 (early) and between 2457700.29-31 (late). The considerable overall scatter in calculated mid-transit times suggests that simultaneous fitting at least in this instance is inadvisable. No connection between individual detrending parameters and whether the calculated mid-transit time would be in the "early" or "late" group was observed.

WASP-103b

Observations were made of WASP-103b on May 17 from 06:02:08 until 09:49:54 UT. The predicted transit start, middle and end times were 06:28, 7:46 and 09:04 UT, respectively, and full coverage of the transit is expected. An exposure length of 110 seconds determined as ideal for the evening and the CCD was cooled to -30º C. Morning twilight on May 17 began at 08:21 UT, and so observations of the egress and off-transit after egress were made under slowly increasing light conditions. The moon was at 74% illumination (i.e. waxing gibbous) but was never closer than 73 degrees in the sky to the target. This observation was the second transit ever observed for this project, and was subject to full automatic calibration, including scaled dark and flat correction. No subsequent calibration beyond the automatic took place. A meridian flip occurred at approximately 07:18 UT and halted image acquisition for 15 minutes.

The predicted mid-transit time for WASP-103b on May 17 was 7:46 UT, or 2457525.8298 BJD. The ideal detrending function was a time-dependent linear function and yielded a mid-transit time of 2457525.8290 +/- 0.0010 BJD which agrees with the predicted value (Figure 17). The data was explored further by detrending by the best systematic parameters, which were the X-center, PSF, airmass and background values, and yielded a mid-transit time of 2457525.8300 +/- 0.0010 BJD (Figure 18). These results corroborate the trend on ETD for WASP-103b which indicates that no significant drift in transit timing is occurring (Figure 19).

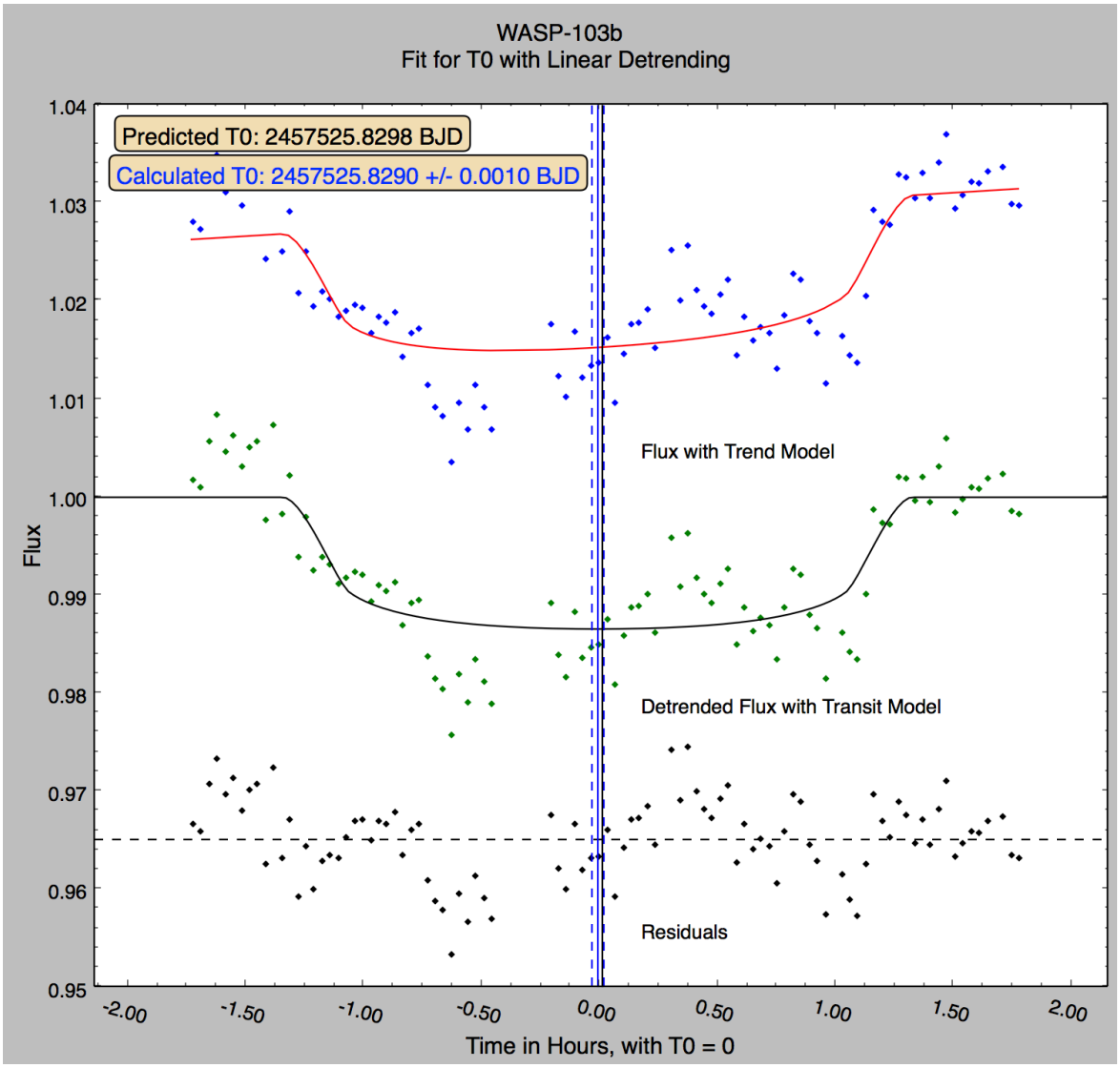

Figure 17. Time dependent detrending using a linear function for WASP-103b. Calculated values for mid-transit time (blue line) are consistent with the predicted value (black).

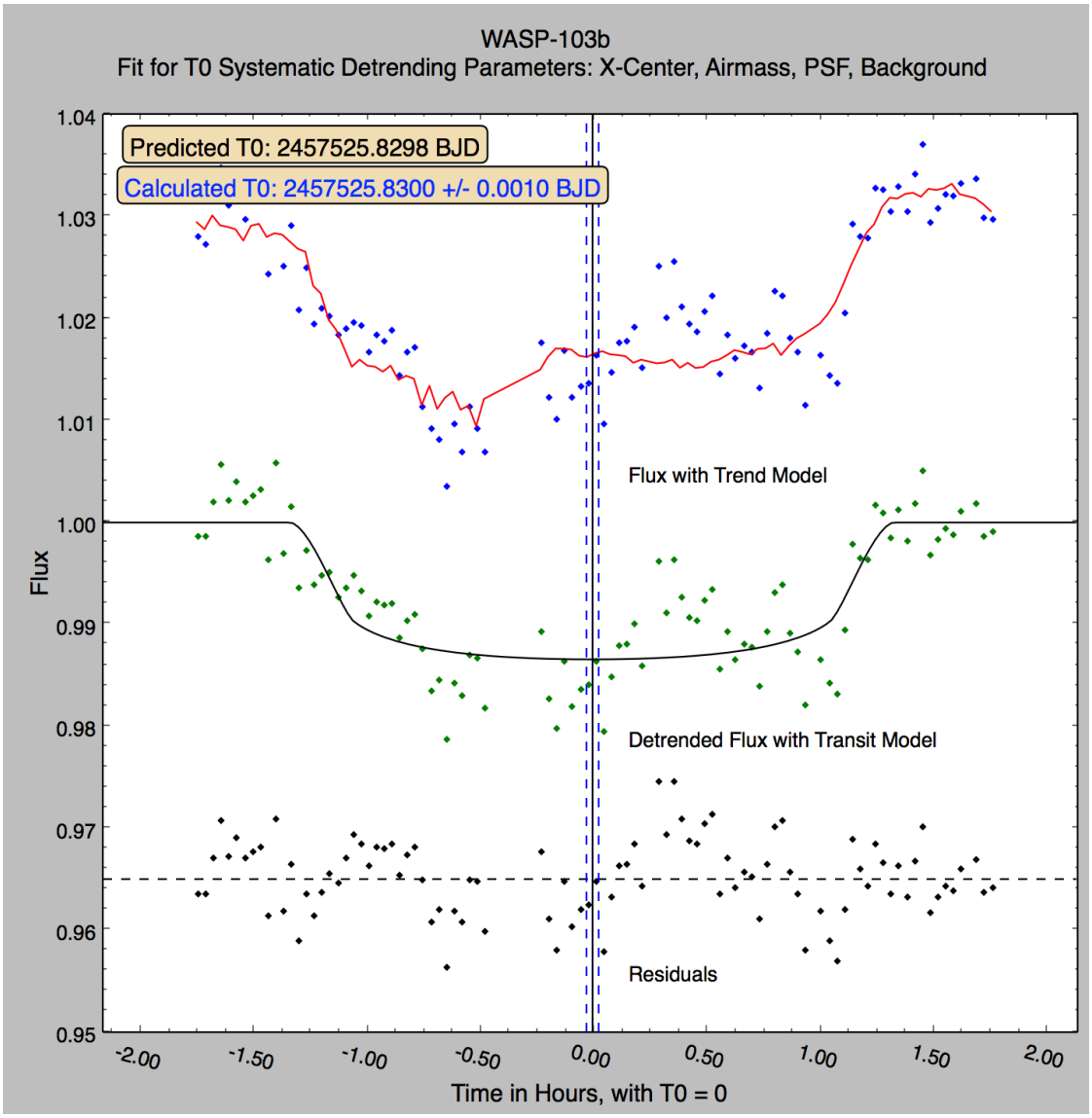

Figure 18. Transit of WASP-103b fit for mid-transit time (T0) after systematic detrending. Parameters used were the X-center, airmass, PSF, and background.

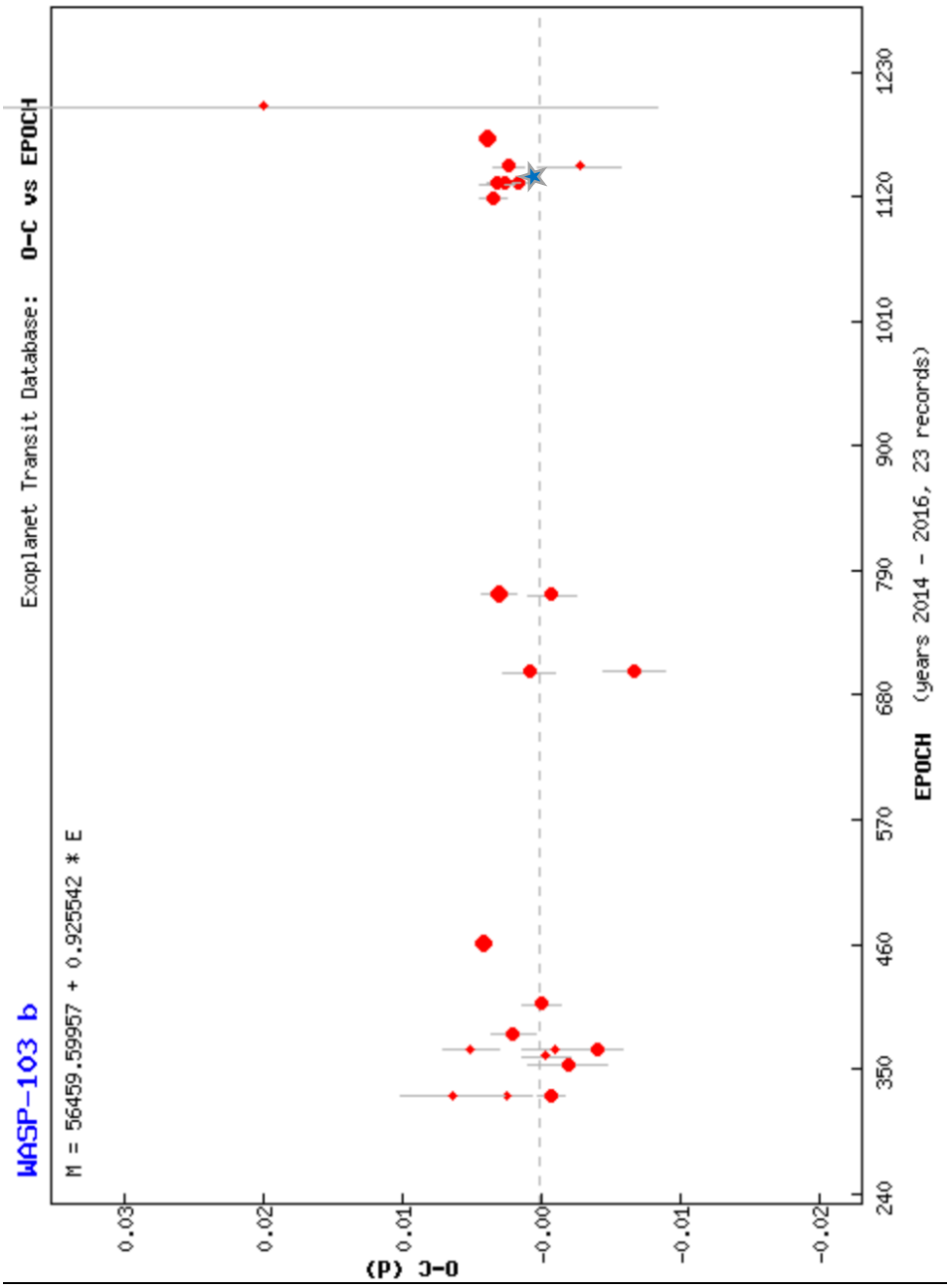

Figure 19. O-C diagram for WASP-103b made from data available on ETD. The blue star represents approximately where the data gathered for this research would plot [059].

HAT-P-16b

HAT-P-16b was not on the original target list. However, the recently recovered Internet Observatory #3 (IO3) was ready on the evening of October 12, and in order to take advantage of clear skies, this target was selected from a list of predicted transits.

With great chagrin and slight amusement, it was realized that observations of the stellar host for HAT-P-16b in fact took place on the wrong evening. This error was the result of a misreading of predicted transits that were listed as "UT evening dates". This was interpreted as the times in UT for the transit but were really "the night of" the given date. As a result, the transit that occurred on Oct 14 UT (the night of Oct 13) was thought to occur on Oct 13 UT (the night of Oct 12).

Nevertheless, this provides an opportunity to realize the dangers of assuming the desired signal is actually present in noisy data instead of objectively reviewing the data as it is and allows for a comparison between the time-dependent and systematic detrending in a general case of "flat" flux with no transit signal present.

Observations were made of HAT-P-16b using IO3 at 30 second exposures in the Clear-filter and the CCD was cooled to -30ºC. The predicted start, middle and end times of the transit were 07:04 UT, 8:36 UT and 10:02 UT, respectively. Observations began at 06:11 UT and concluded at 09:20 UT as insurmountable clouds rolled in, halted observing for that evening and rendered useless the last half hour of exposures. This was also substantially earlier than required in order to get full out-of-transit coverage. Dark and flat field calibration were performed and no meridian flip took place.

Inspection of the normalized flux reveals a small gap after which the flux values shift significantly (Figure 20). It is possible that this shift is due to the transit egress

occurring exactly when the gap in observations occurred. However, comparison of the predicted transit time vs. observation time, knowledge that there is in fact no transit occurring on the night this data was taken, and a look at the systematic detrending parameters reveals that it is more likely a result of inter-pixel variations as the FOV shifted on the CCD. The gap itself was caused by a sudden and inexplicable loss of adequate focus (probably mirror flop), the recovery of which necessitated a pause in observing.

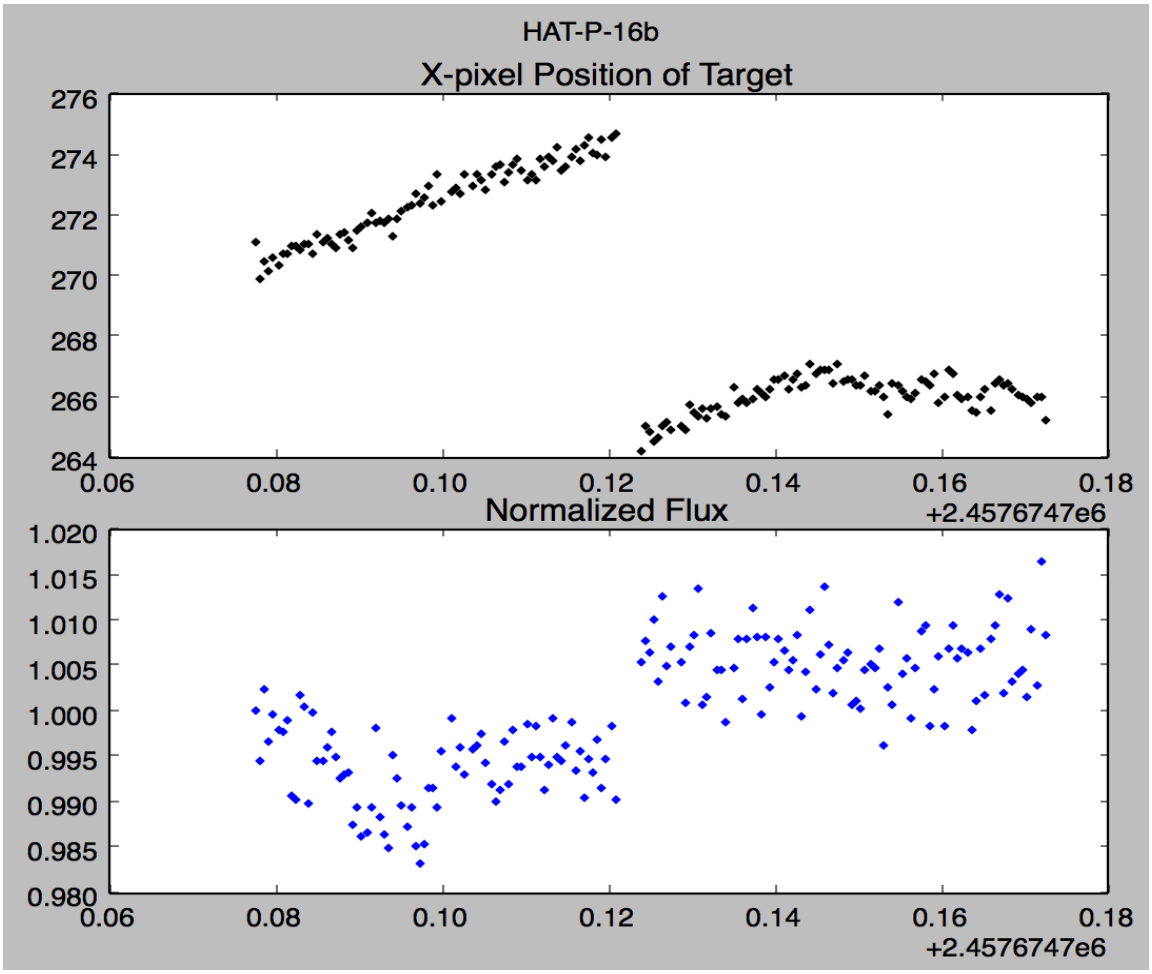

Figure 20. X-pixel position and normalized flux values for HAT-P-16b. Top: The X-pixel center position of the target for each image of HAT-P-16b. Bottom: The normalized flux of the target for each image. The gap and subsequent shift in flux values can be accounted for by the shift of the FOV on the CCD, described here by the shift in X-pixel position.

Both time-dependent and systematic detrending were applied to the light curve, and the time-dependent detrending function was simply unable to account for the gap and the shift. Systematic detrending was implemented and the x/y-center and background sky values were identified as the best parameters that could account for the shift, some of the scatter, and other instrumental effects (Figure 21). It is perhaps encouraging that the transit was fit in such a way that the flattest part of the transit curve was fit to data that should be flat to begin with, considering no transit or known variation is present.

The dangers of poor transit coverage and a willingness to see patterns in data that may not be there are exemplified in this case by the fact that a transit was able to be fit to data in which there was no transit taking place. The result of these errors caused slight but important changes in the modeling procedure, specifically in changing how the mid-transit time was initialized. At first, the mid-transit time was set to the halfway point of the timestamps of observations, which makes the assumption that observations occurred on the correct evening and also that the transit occurred near enough to when it was predicted to be observed at all. This was remedied by initializing the mid-transit time to the actual predicted mid-transit time converted to BJD. In terms of code, this removes a small element of generalizability for the sake of accuracy – a small price to pay in tedium for an essential element of veracity.

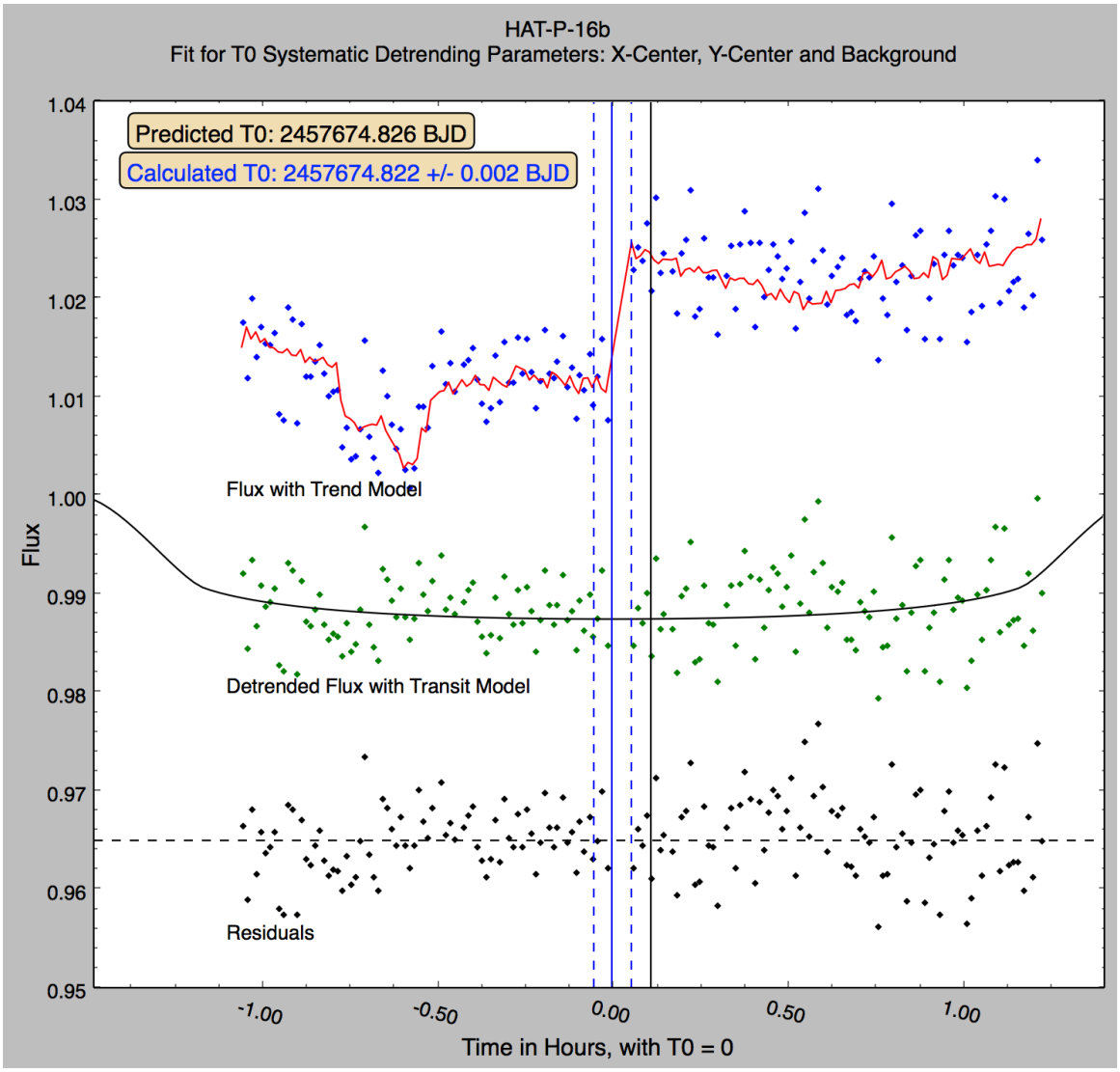

Figure 21. The "fitting" of a non-existent transit for HAT-P-16b. Presented here to illustrate the dangers of assuming a feature is present in noisy data. Without knowing observations of the target took place at the wrong time, this poorly fit transit is consistent with what was expected of the transit in light of incomplete transit coverage due to clouds. Also shown to illustrate how a shift in the raw normalized flux (top) can be accounted for by systematic detrending and "smoothed out" (middle).

WASP-48b

Observation of WASP-48b was performed from Aug 6 04:15 UT until 09:08 UT. Predicted transit start, middle and end times were 5:24 UT, 6:59 UT and 8:35 UT, respectively. Exposures were 60 seconds in the R-filter, and required calibration by flats only. The CCD camera was cooled to -25º C. A meridian flip occurred early in observing, at 04:47 UT and halted observing for 13 minutes. However, the first 25 exposures were not used in the detrending and model fitting due to large variations in the focus and thus the gap caused by the meridian flip does not affect the data. Full coverage of the transit is expected and was apparently achieved.

Systematic detrending was superior to time-dependent, with parameters X-center, PSF and airmass providing the best fit to the data. The fit for mid-transit time yielded T0 = 2457606.7935 +/- 0.0013 BJD, which matches the predicted value of T0 = 2457606.7933 BJD within one standard deviation (Figure 22). Time dependent detrending was also performed for consistency, and yielded a slightly later T0 of 2457606.8008 +/- 0.0020 BJD. (Figure 23), corresponding to a difference of approximately 10 minutes. The results of both detrending schemes are shown on the O-C plot from ETD in Figure 24. This set of data, along with WASP-103b, is among the better reduced and higher quality sets attained for this research, relatively speaking. Despite the scatter in the overall data it may be permissible to have higher confidence in the results of this analysis in light of full transit coverage and decent cadence.

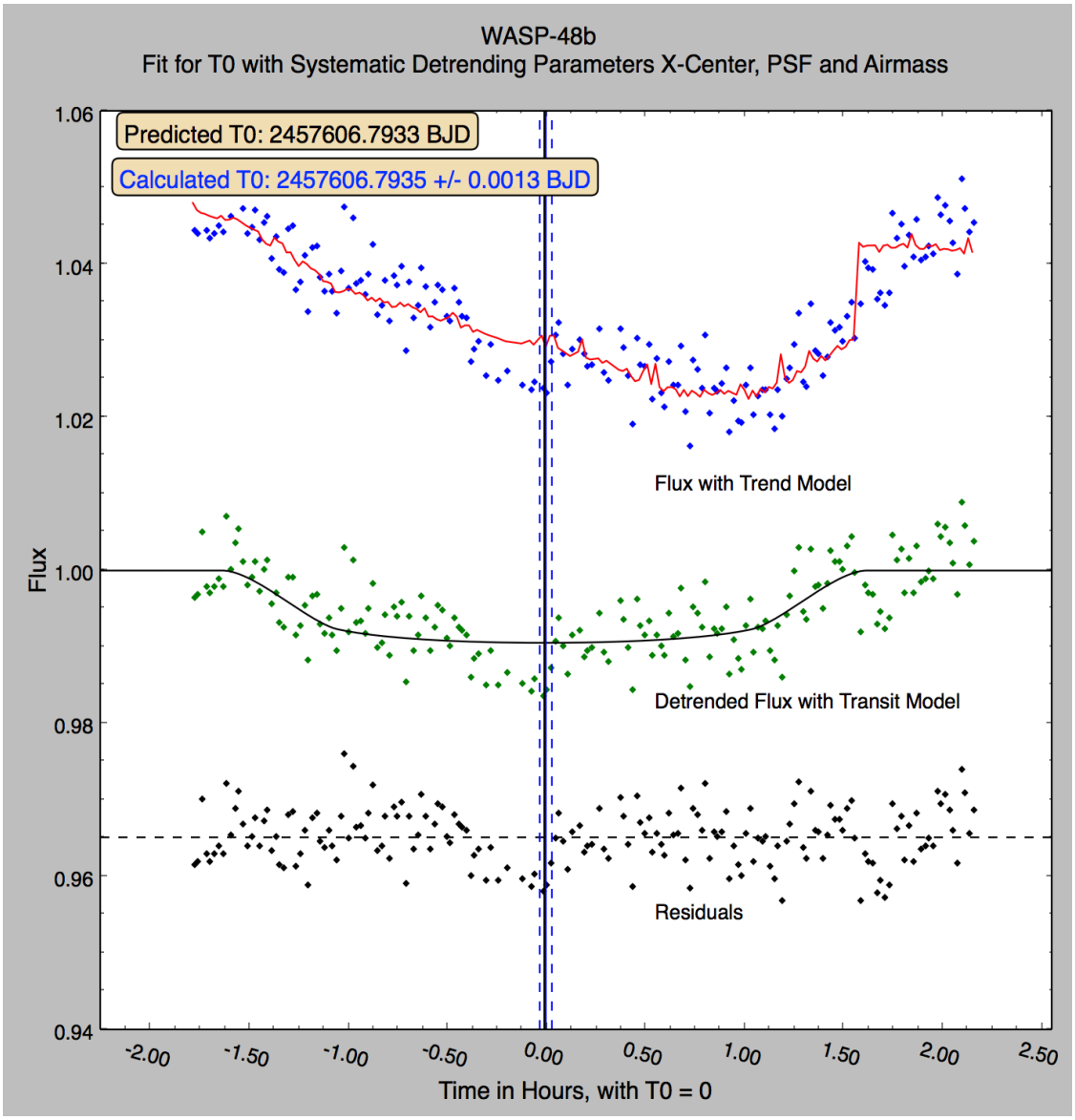

Figure 22. Transit fit for mid-transit time using systematic detrending of WASP-48b. In this case, the predicted (black line) and calculated (blue lines) times are so close as to be indistinguishable in the middle plot. 1σ errors are represented as the dotted blue lines.

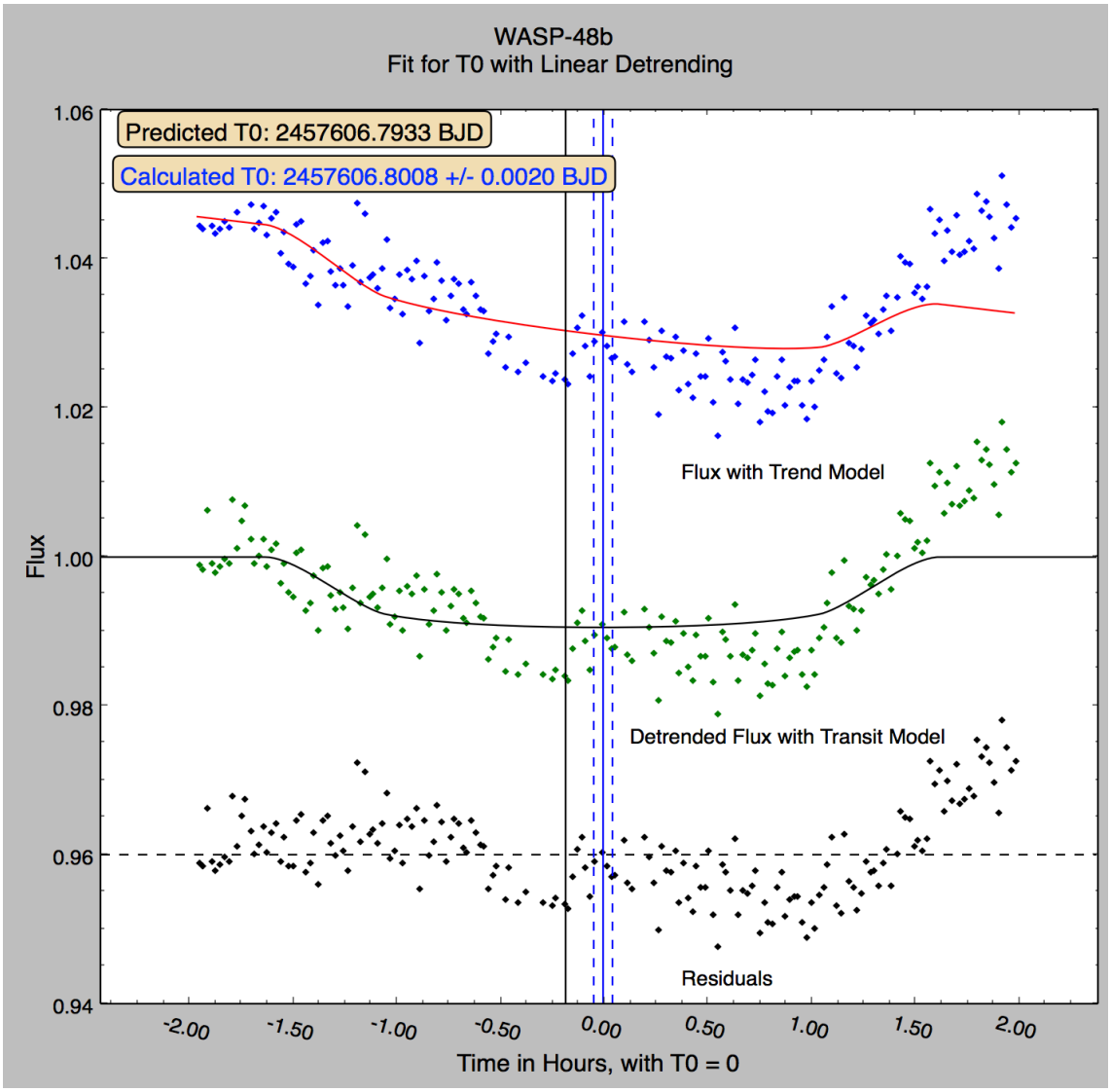

Figure 23. Transit fit for mid-transit time of WASP-48b after time-dependent detrending by a linear function.

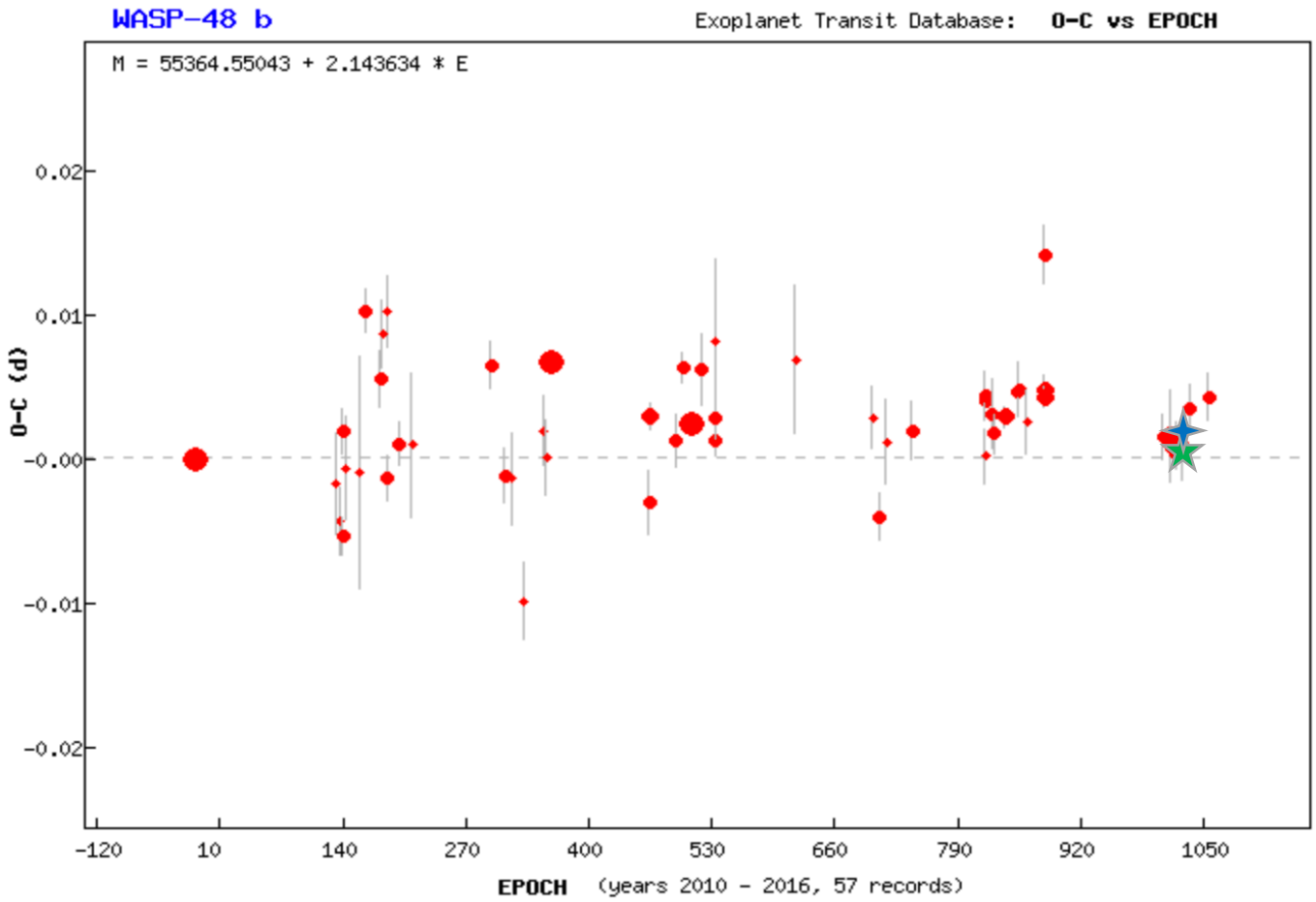

Figure 24. O-C diagram made from the dataset available on ETD for WASP-48b. The green five pointed star represents approximately where the mid-transit time calculated after systematic detrending (Figure 5.11) would plot, and the four-pointed star represents where the mid-transit time calculated using linear time-dependent detrending (Figure 5.12) would plot [059].

CHAPTER VI

CONCLUSIONS, RECOMMENDATIONS FOR FUTURE RESEARCH

Despite the excess of difficulties encountered at seemingly every step of the process, the results that were ultimately obtained are valuable just as much for the modest levels of success that were realized as where the results fell short. The difficulties in instrumentation and the systematic disruptions introduced into the data corroborate the value of applying systematic-based detrending to recover light curves for ground-based TTV efforts as noted by Essen et al. (2016) [052].

Essen et al. (2016) analyzed simulated transits of a hot Jupiter with properties based on real-world exoplanet Qatar-1 b both with and without an Earth-size perturbing exterior planet in a 3:2 mean motion resonance. Further, they simulate what the light curve for the hypothetical planet would look like at ground-based observatories when typical sources of instrumental and environmental noise are injected into the data. Once the light curves and associated noise are simulated, the light curves are analyzed in an attempt to recover the original system parameters as well as assess the possibility and parameters of a non-transiting planet by TTV analysis. This analysis includes normalization and detrending separately by both a low order time-dependent function and a linear combination of systematic or instrumental factors, specifically airmass, seeing, x/y pixel position and integrated flat counts.

Many of the results of the simulations are relevant to this project and directly inform recommendations for future research. One such finding is that detrending based on

instrumental factors is better able to produce more accurate and consistent determination of transit parameters, including mid-transit time. A second key finding is that the use of incomplete or poorly covered transits leads to large timing variations that are independent of any real, celestial phenomenon. Therefore, in order to have a chance at using ground-based observatories to conduct TTV analysis, complete transit coverage with good cadence, or high number of exposures, at sufficient photometric quality are a requirement. As has already been stated, these qualities were rarely fulfilled adequately during the current research project, if at all.

Further, the problems introduced by the automatic calibration, target drift and meridian flip motivated an exploration of the capabilities of the UND Internet Observatory, and several solutions have been implemented. These refinements include minor adjustments to the pointing model of IO1 and IO3 to prevent target drift and enabling the Paramount ME German Equatorial Mount (GEM) to image up to and slightly past the meridian to minimize lost time for the meridian flip. This option is not available on all GEMs, but should be taken advantage of whenever safely possible.

The transits of WASP-48b and WASP-103b were two of the higher quality datasets, had calculated mid-transit times consistent with predictions and are tentatively consistent with the existing dataset on ETD. Nonetheless, several recommendations can be made in order to increase the odds of successful TTV and other exoplanet observing projects in the future:

1) Transits should be observed for the entire night on which they occur instead of merely an hour before and after predicted start and end times. This will minimize issues of insufficient transit coverage caused by delayed observatory initialization, faulty predictions and real transit timing variations.
2) Flat fields should be taken on both sides of the meridian. This is to ensure that images taken on both sides of the meridian that introduce and scatter light in slightly different ways, and a CCD that has been rotated 180°, can be accurately calibrated.
3) Keep observing! A more robust TTV analysis requires a longer baseline of accurate observations.

Even though the current research was unable to produce highly reliable data, there is every reason to believe that the data that could be produced in the near future will be superior. As the operator's technique and understanding of observatory processes and analysis procedure continues to develop, there is no doubt that more contributions can be made to the search and exploration of exoplanetary systems by this method in the future.

REFERENCES

[01] Gillon, M., Triaud A.H.M.J., Demory, B.O., Jehin, E., Agol, E., Deck, K.M., . . . Queloz, D. (2017). Seven temperate terrestrial planets around the nearby ultracool dwarf star TRAPPIST-1. *Nature, 542*(7642), 456.

[02] Lissauer, J. (2002). Extrasolar planets. *Nature*, *419*(6905), 355-358.

[03] Wolszczan, A., Frail, D.A. (1992). A planetary system around the millisecond pulsar PSR 1257+12. *Nature 355*(6356):145-7.

[04] Pepe, F., Ehrenreich, D., Meyer, M. R. (2014). Instrumentation for the detection and characterization of exoplanets. *Nature, 513*(7518), 358-366.

[05] Mayor, M., Queloz, D. (1995). A Jupiter-mass companion to a solar-type star. *Nature 378* (6555): 355–359.

[06] Latham, D. W. (2012). The unseen companion of HD 114762. *New astronomy reviews, 56*(1), 16-18.

[07] Latham, D. W., Mazeh, T., Stefanik, R. P., Mayor, M., & Burki, G. (1989). The unseen companion of HD114762: a probable brown dwarf. *Nature, 339*(6219), 38-40.

[08] Perryman, M. (2011). Exoplanet Handbook. Leiden: Cambridge University Press.

[09] Wilson, R. E. (1953). General Catalogue of Stellar Radial Velocities. *Astrophysical Journal* 119, p. 689.

[010] Griffin, R. and Griffin, R. (1973) Accurate wavelengths of stellar and telluric absorption lines near lambda 7000 Angstroms. *Mon. Not. Roy. Astr. Soc*., *162*, 255-260.

[011] Campbell, B. and Walker, G. A. H (1979) Precision radial velocities with an absorption cell. *Publ. Astron. Soc. Pac*., *91*, 540-545.

[012] Lovis, C., & Fischer, D. (2010). Radial velocity techniques for exoplanets. *Exoplanets*, 27-53.

[013] Marcy, G. (1992). Precision radial velocities with an iodine absorption cell (for generating reference absorption lines in stellar spectra). *Publications of the Astronomical Society of the Pacific, 104*(674), 270-277.

[014] Butler, R.P., Marcy, G.W., Fischer, D.A., et al. (1999). Evidence for multiple companions to υ And. *ApJ, 526*, 916–927.

[015] Curiel, S., J. Cantó, J., Georgiev, L., Chávez, C. E., and Poveda, A. (2011). A fourth planet orbiting υ Andromedae. *A&A, 525*, A78.

[016] Henry, G. W., Marcy, G. W., Butler, R. P., Vogt, S. S. (1999). A transiting "51 peg-like" planet. *Astrophysical Journal, 529*:L41-L44.

[017] Queloz, D., Mayor, M. (2001). From CORALIE to HARPS: The way towards 1ms precision Doppler measurements. *The Messenger*, *105*, 1-7.

[018] Bouchy, F., and The Sophie Team (2006) SOPHIE: the successor of the spectrograph ELODIE for extrasolar planet search and characterization. In *Tenth Anniversary of 51 Peg-b: Status of and prospects for hot Jupiter studies* (L. Arnold et al., eds.), 319-325.

[019] Mayor, M., Pepe, F., Queloz, D., et al. (2003) Setting New Standards with HARPS. *The Messenger*, *114*, 20-24.

[020] Butler, R. P., Tinney, C. G., Marcy, G. W., Jones, H. R., Penny, A. J., & Apps, K. (2001). Two new planets from the Anglo-Australian planet search. *The Astrophysical Journal*, *555*(1), 410.

[021] McArthur, B. E., Endl, M., Cochran, W. D., Benedict, G. F., Fischer, D. A., Marcy, G. W., ... & Udry, S. (2004). Detection of a Neptune-mass planet in the ρ1 Cancri system using the Hobby-Eberly Telescope. *The Astrophysical Journal Letters*, *614*(1), L81.

[022] Butler, R. P., Vogt, S. S., Marcy, G. W., Fischer, D. A., Wright, J. T., Henry, G. W., ... & Lissauer, J. J. (2004). A Neptune-mass planet orbiting the nearby M dwarf GJ 436. *The Astrophysical Journal*, *617*(1), 580.

[023] Lovis, C., Mayor, M., Pepe, F., Alibert, Y., Benz, W., Bouchy, F., ... & Santos, N. C. (2006). An extrasolar planetary system with three Neptune-mass planets. *Nature*, *441*(7091), 305-309.

[024] Valencia, D.,Sasselov, D., & O'Connell, R. J. (2007). Radius and Structure Models of the First Super-Earth Planet. *Astrophysical Journal, 656*(1), 545-551.

[025] Tuomi, M., Anglada Escudé, G., Gerlach, E., Reiners, Reiners, A., ... Butler, R. P. (2013). Habitable-zone super-Earth candidate in a six-planet system around the K2.5V star HD 40307. *Astronomy and Astrophysics, 549*, A48.

[026] Barnes, R., Jackson, B., Raymond, S. N., West, A., & Greenberg, R. (2009). The HD 40307 planetary system: super-Earths or mini-Neptunes?. *Astrophysical Journal, 695*(2), 1006-1011.

[027] Haswell, C. A. (2010). *Transiting exoplanets* (1st ed.). Cambridge: Cambridge University Press.

[028] Charbonneau, D., Brown, T. M., Latham, D. W., & Mayor, M. (2000). Detection of planetary transits across a sun-like star. *Astrophysical Journal, 529*(1), L45-L48.

[029] Udalski, A., Paczynski, B., Zebrun, K., et al. (2002). The Optical Gravitational Lensing Experiment. Search for Planetary and Low-Luminosity Object Transits in the Galactic Disk. Results of 2001 Campaign. *Acta Astronomica. 52* (2): 115–128.

[030] Street, R. A., Pollaco, D. L., Fitzsimmons, A., Keenan, F. P., Horne, K., Kane, S., ... & Jones, B. W. (2003). SuperWASP: wide angle search for planets. *Scientific Frontiers in Research on Extrasolar Planets. 294*, 405-408.

[031] Pepper, J., et al. (2007). "The Kilodegree Extremely Little Telescope (KELT): A Small Robotic Telescope for Large-Area Synoptic Surveys". *Publications of the Astronomical Society of the Pacific*. *119* (858): 923–935.

[032] Alonso, R., Brown, T., Torres, G., Latham, D., Sozzetti, A., Mandushev, G., . . . Stefanik, R. (2004). TrES-1: The Transiting Planet of a Bright K0V Star. *Astrophys.J. 613* (2004) L153-L156.

[033] Bakos, G. Á.; et al. (2002). System Description and First Light Curves of the Hungarian Automated Telescope, an Autonomous Observatory for Variability Search. *Publications of the Astronomical Society of the Pacific. 114* (799): 974–987.

[034] Russell, D. (2013). Solar and Extrasolar Planet Taxonomy. *arXiv preprint arXiv:1308.0616*.

[035] Hatzes, A. P. (2014). The role of space telescopes in the characterization of transiting exoplanets. *Nature, 513*(7518), 353-357.

[036] Batalha, N. M. (2014). Exploring exoplanet populations with nasa. *Proceedings of the National Academy of Sciences of the United States of America, 111*(35), 12647.

[037] Johnson, M. (n.d.). Exoplanet Count. Retrieved December 14, 2015, from http://www.nasa.gov/mission_pages/kepler/main/index.html

[038] NASA Exoplanet Archive. Retrieved April 16, 2016, from http://exoplanetarchive.ipac.caltech.edu/.

[039] Charbonneau, D.,Brown, A., & Burrows, G. (2006). When extrasolar planets transit their parent stars. Cornell University.

[040] "5. Identifying, Exploring and Characterizing Environments for Habitability and Biosignatures." NASA Astrobiology Strategy 2015. Ed. Lindsay Hays. 2015. Pp 90 – 120.

[041] Rice, K. (2014). The detection and characterization of extrasolar planets. *Challenges*, *5*(2), 296-323.

[042] Planetary Habitability Laboratory at UPR Arecibo. (2010). Retrieved December 14, 2015, from http://phl.upr.edu/home.

[043] Holman, M. J., & Murray, N. W. (2005). The use of transit timing to detect terrestrial-mass extrasolar planets. *Science*, *307*(5713), 1288-1291.

[044] Steffen, J. H., Gaudi, B. S., Ford, E. B., Agol, E., & Holman, M. J. (2007). Detecting and Characterizing Planetary Systems with Transit Timing. *arXiv preprint arXiv:0704.0632*.

[045] Steffen, J. H., Fabrycky, D. C., Agol, E., Ford, E. B., Morehead, R. C., Cochran, W. D., ... & Caldwell, D. A. (2013). Transit timing observations from Kepler–VII. Confirmation of 27 planets in 13 multiplanet systems via transit timing variations and orbital stability. *Monthly Notices of the Royal Astronomical Society*, *428*(2), 1077-1087.

[046] Holman, M. J., Fabrycky, D. C., Ragozzine, D., Ford, E. B., Steffen, J. H., Welsh, W. F., ... & Batalha, N. M. (2010). Kepler-9: A system of multiple planets transiting a Sun-like star, confirmed by timing variations. *Science*, *330*(6000), 51-54.

[047] Agol, E., Steffen, J., Sari, R., & Clarkson, W. (2005). On detecting terrestrial planets with timing of giant planet transits. *Monthly Notices of the Royal Astronomical Society, 359*(2), 567-579.

[048] Patra, K. C., Winn, J. N., Holman, M. J., Yu, L., Deming, D., & Dai, F. (2017). The Apparently Decaying Orbit of WASP-12. *arXiv preprint arXiv:1703.06582*.

[049] Hoyer, S., Pallé, E., Dragomir, D., & Murgas, F. (2016). Ruling out the orbital decay of the WASP-43b exoplanet. *The Astronomical Journal, 151*(6), 8.

[050] Wilkins, A. N., Delrez, L., Barker, A. J., Deming, D., Hamilton, D., Gillon, M., & Jehin, E. (2017). Searching for Rapid Orbital Decay of WASP-18b. *The Astrophysical Journal Letters*, *836*(2), L24.

[051] Essen, C.V., Miculan, R., Paez, R.I. (2013). Oribtal parameter refinement and transit timing variation analysis of the hot-Neptune Gliese 436b. *Asociacion Argentina de Astronomia*, 56.

[052] Essen, C.V., Cellone, S., Mallonn, M., Tingley, B., Marcussen, M. (2016). Modelling systematics of ground-based transit photometry I. Implications on transit timing variations. *Astronomy and Astrophysics*. *arXiv preprint arXiv:1607.03680*.

[053] Howell, S. B. (2006). *Handbook of CCD astronomy* (Vol. 5). Cambridge University Press.

[054] Kass, R. E., Raftery, A. E. (1995). Bayes Factors. *Journal of the American Statistical Association, 90*(430), 773-795.

[055] Dyson, F. (2004). A meeting with Enrico Fermi. *Nature, 427*(6972), 297-297.

[056] Mandel, K., & Agol, E. (2002). Analytic light curves for planetary transit searches. *The Astrophysical Journal Letters*, *580*(2), L171.

[057] Fabrycky, D.; Tremaine, S. (2007). Shrinking Binary and Planetary Orbits by Kozai Cycles with Tidal Friction. *Astrophysical Journal 669*: 1298–1315.

[058] Claret, A. (2000). A new non-linear limb-darkening law for LTE stellar atmosphere models: Calculations for -5.0 ≤ log[M/H] ≤ 1,2000 K ≤ T eff ≤ 50000 K at several surface gravities. *Astronomy and astrophysics*, *363*(3), 1081-1090.

[059] Poddany, S., Brat, L., Pejcha ,O. (2010) Exoplanet Transit Database. Reduction and processing of the photometric data of exoplanet transits. *New Astronomy 15*, 297 - 301. arXiv:0909.2548v1.

[060] Sorenson, P., Azzaro, M., & Mendez, J. (2002). Isaac Newtan Group of Telescopes. Retrieved from http://www.ing.iac.es/.

[061] Tody, D. (1986) The IRAF data reduction and analysis system. *Proc. SPIE Instrumentation in Astronomy VI, ed. D.L. Crawford, 627*, pp. 733.

[062] Eastman, J., Siverd, R., Gaudi, S. B. (2010). Achieving better than 1 minute accuracy in the heliocentric and barycentric julian dates. *Publications of the Astronomical Society of Pacific*, *122* (894), pp. 935.

[063] Vargha, M., & Kolláth, Z. (1999). The first century of Konkoly Observatory. *Astronomy & Geophysics*, *40*(5), 5-17.

[064] Johnson, M. (2015, March 31). Kepler and K2 Missions. Retrieved April 24, 2017, from https://www.nasa.gov/mission_pages/kepler/main/index.html

[065] *Mercury Transit 08 November 2006* [Photograph found in Solar and Heliophysics Observatory (SOHO) Hotshots, NASA, Https://soho.nascom.nasa.gov/ hotshots/index.html/]. (n.d.). Retrieved from https://soho.nascom.nasa.gov/ hotshots/index.html/ (Originally photographed 2006, November 8)

[066] Schneider, J., Dedieu, C., Le Sidaner, P., Savalle, R., & Zolotukhin, I. (2011). Defining and cataloging exoplanets: the exoplanet.eu database. *Astronomy & Astrophysics*, *532*, A79.

[067] Miles, R. (2007). A light history of photometry: from hipparchus to the hubble space telescope. *Journal of the British Astronomical Association*, *117*, 172-186.

[068] Bond, W. C. (1857). *Observations on the Planet Saturn: Made with the Twenty-three Foot Equatorial, at the Observatory of Harvard College, 1847-1857* (Vol. 2). Metcalf, printers to the University.

[069] Hubble, E. P. (1925). Cepheids in spiral nebulae. *Popular Astronomy*, *33*.

[070] Monet, D. G., Levine, S. E., Canzian, B., Ables, H. D., Bird, A. R., Dahn, C. C., ... & Levison, H. F. (2003). The USNO-B catalog. *The Astronomical Journal, 125*(2), 984.

[071] Stebbins, J. (1910). The measurement of the light of stars with a selenium photometer, with an application to the variations of Algol. *The Astrophysical Journal*, *32*.

[072] Kron, G. E. (1939). Determination of the coefficient of limb darkening for the eclipsing variable YZ (21) Cassiopeiae. *Lick Observatory Bulletin*, *19*, 59-71.

[072] Baum, W. A. (1954). Globular clusters. II. The tentative identification of the main sequence of population II from photoelectric observations in M 13. *The Astronomical Journal*, *59*, 422-432.

[073] Koch, D. G.,W. J., Borucki, G., Basri, N. M., Batalha, T. M., Brown, D., ... Wu, H. (2010). Kepler Mission design, realized photometric performance, and early science. *The Astrophysical Journal Letters, 713*(2), L79-L86.

[074] Borucki, W. J. (2016). KEPLER Mission: Development and overview. *Reports on Progress in Physics, 79*(3), 036901.